FREQUENCY COMB EXPERIMENTS AND RADIO FREQUENCY INSTRUMENTATION ANALYSIS FOR OPTICAL ATOMIC CLOCKS
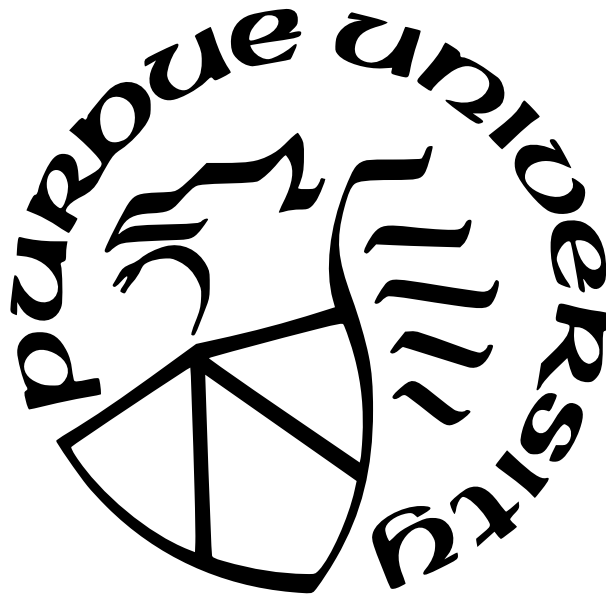
by

Ryan Schneider

A Thesis

Submitted to the Faculty of Purdue University

In Partial Fulfillment of the Requirements for the degree of

Master of Science in Electrical and Computer Engineering

School of Electrical and Computer Engineering

West Lafayette, Indiana

December 2022

THE PURDUE UNIVERSITY GRADUATE SCHOOL
STATEMENT OF COMMITTEE APPROVAL

Dr. Andrew M. Weiner, Chair

School of Electrical and Computer Engineering

Dr. Jason McKinney

School of Electrical and Computer Engineering

Dr. Minghao Qi

School of Electrical and Computer Engineering

Dr. Mark Bell

School of Electrical and Computer Engineering

Approved by:

Dr. Dimitrios Peroulis

ACKNOWLEDGMENTS

In order to complete this thesis, I needed a great team to provide support and expertise. First of all, I would like to thank Professor Weiner for being my advisor, a great mentor, and being willing to accommodate my military timeline and other requirements. The contributions by Professor McKinney, Professor Qi, and Professor Bell are greatly appreciated and helped make this educational experience even more valuable. In addition, I would like to thank Dr. Cong Wang, Dr. Kaiyi Wu, and Nathan O'Malley for their guidance and assistance with my experiments. I would also like to thank the other members of my lab group for their friendship, mentorship, and helping me navigate the challenges of graduate school and research.

Next, I would like to thank the Purdue Military Research Institute, most notably Colonel Dave Hankins and Dr. Eric Dietz, for my fellowship funding and their continued support of graduate research for military students. I would also like to thank my roommates Winnie Chen and Robert Pekarek, in addition to the other US military officers at Purdue for their friendship and support. I also appreciate the United States Air Force and United States Space Force giving me the opportunity to complete my education before I return to active duty.

Finally, I would like to thank my family back in Colorado for teaching me to never give up and instilling a desire to learn more and serve my nation. Without their continued support, I would never have made it this far.

TABLE OF CONTENTS

LIST OF TABLES

LIST OF FIGURES

ABBREVIATIONS

PPLN	Periodically Poled Lithium Niobate
TDFA	Thulium Doped Fiber Amplifier
SHG	Second Harmonic Generation
RF	Radio Frequency
FFT	Fast Fourier Transform
DSA	Digital Signal Analyzer
ESA	Electronic Spectrum Analyzer
RBW	Resolution Bandwidth
SNR	Signal to Noise Ratio

ABSTRACT

Space-based global navigation and precision timing systems are critical for modern infrastructure. Atomic clock technology has increased the precision of these systems so that they are viable for military operations, navigation, telecommunications, and finance. Advances in optical atomic clocks, based on optical frequencies, provide an opportunity for even more precise timing. Therefore, developments in chip-scale optical atomic clock technologies could lead to increased and more wide-spread application of this precision timing. One component of the optical atomic clock is the optical frequency comb which serves as an interface between optical and microwave frequencies. This thesis will cover experiments related to these optical frequency combs. A 2μm fiber laser was developed in order to test second harmonic devices required to stabilize an optical frequency comb. The laser was then employed to measure the operating wavelengths and efficiencies of non-linear devices. In addition, an analysis of the radio frequency instruments used to evaluate microwave outputs was conducted to determine whether a digital signal analyzer (oscilloscope) or an analog electronic spectrum analyzer provides more accurate results for optical frequency comb based experiments.

1. INTRODUCTION

1.1 Overview

1.1.1 Optical Atomic Clocks and Global Navigation Applications

For decades the industry standard for precision timing has been the atomic clock which uses an atomic transition as a reference [1], [2]. Innovations in microwave electronics have miniaturized these systems so that they can be integrated onto spacecraft, which provides precision timing to the military, private industry, and individual consumers. Widely used systems such as the US military's Global Positioning System (GPS) and the European Space Agency's Galileo constellation use radio frequency atomic clocks to disseminate precise timing and location all around the world. While current infrastructure utilizes radio frequencies in order to denote time, optical atomic clocks, which utilize higher optical frequencies, measure atomic transitions even more precisely. Since time is the inverse of frequency, higher frequencies result in smaller time intervals that can be resolved.

In laboratory settings, optical atomic clocks have demonstrated up to three orders of magnitude better stability (meaning that they do not drift over time) than conventional microwave atomic clocks [3]. Such improvements in the timing stability provide benefits to many applications including position, navigation, and timing (PNT), fundamental science experiments, and astronomy [4]–[6]. For the United States Department of Defense, local, independent, and compact optical atomic clock systems could provide position, navigation, and timing in GPS denied environments [7].

While a research group at the National Institute of Standards and Technology (NIST) built a proposed chip-scale optical atomic clock architecture [5], many other proposed systems have not reached the technology readiness level (TRL) required for flight testing and adoption [3]. For this reason, the United States Department of Defense and the United States Space Force benefit from research and development into miniaturized and more stable optical atomic clocks that can be integrated into fieldable systems.

1.1.2 Fundamentals of Optical Atomic Clocks

Optical atomic clocks contain three major components for operation. The first is a stable laser that functions as an oscillator. This oscillator serves as the time reference for the clock. The second component is an atomic reference that stabilizes the laser cavity of the oscillator to ensure that the timing reference does not drift long term. The laser cavity and atomic reference can be configured in multiple ways, but further discussion of these is beyond the scope of this thesis [2], [3], [8]. The third component is an optical frequency comb which serves as a interface between optical frequencies of the timing reference and the microwave frequencies that can be read by conventional electronics [2], [4], [9]. Much of the discussion in this thesis will focus on projects related to the development of this optical frequency comb as it pertains to the optical atomic clock.
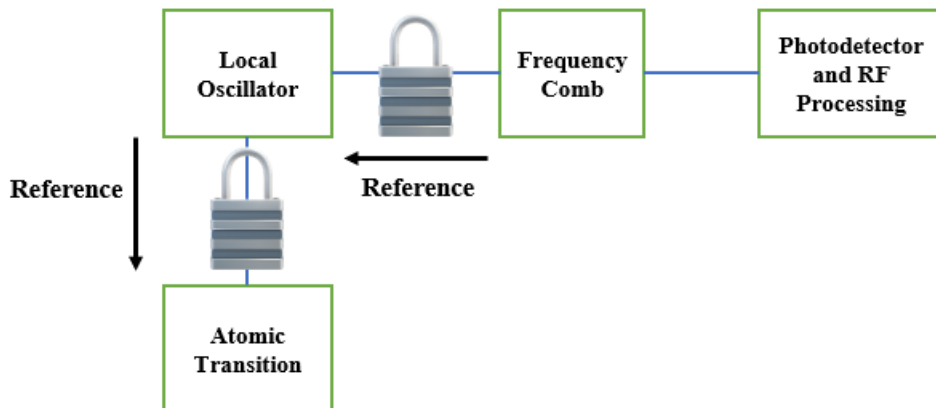
Figure 1.1. High level diagram of the optical atomic clock including the atomic transition, local oscillator, and frequency comb

Currently, optical atomic clocks require laboratory set ups with large and high power electronics to operate. In order to make these clocks more versatile, especially for military applications, the size, weight, and power (SWaP) of these clocks must be improved. As a civil space entity, the European Space Agency provides some data on the SWaP budgets of the Galileo navigation system that can be used as a benchmark for new systems. The more compact microwave atomic clock system has a mass budget of 3.5 kg, a power budget of 35

W and and volume of 3.2 liters. The more robust microwave clock system has a mass budget of 18.2 kg, a power budget of 60 W, and a volume of 26.2 liters [3]. As a result, a viable space bound optical atomic clock would need to match similar performance parameters, while also possessing comparable or better timing precision than existing microwave atomic clocks. A strategy to meet this requirement is to design a photonic integrated circuit that will contain the necessary components for the optical atomic clock in a more compact form. The Atomic-Photonic Integration (A-PhI) program at the Defense Advanced Research Projects Agency (DARPA) seeks to miniaturize optical atomic clock systems without degrading their time keeping performance. As a result, local, independent, and compact optical atomic clocks may serve as a redundant navigation technique that could be deployed in a GPS denied environment [7].

1.2 Optical Frequencies Combs and Their Connection to Optical Atomic Clocks

While higher frequency optical signals ($\sim$100s THz) can provide increased precision to timing systems, microwave electronics (operating at $\sim$10s GHz) are not able to detect such high frequencies. As a result, an interface between these two frequency ranges is required. The solution is the optical frequency comb. Optical frequencies combs are a technology where periodic pulses of light are generated by a mode-locked (pulsed) laser [10]. The equal temporal spacing of these pulses, emitted from the laser, results in equally-spaced lines in the frequency domain. The frequency spacing of these comb lines is referred to as the repetition rate of the frequency comb and is denoted (f_{rep}). The repetition rate is the inverse of the time between pulses emitted from the laser [10]. In addition, the frequency comb -possesses a carrier envelope offset frequency (f_{CEO}) which characterizes the variation in the comb line and the carrier frequency [11]. Equation 1.1 is the frequency comb equation for an arbitrarily selected comb line (n).

$$f_n = n f_{rep} + f_{CEO} \tag{1.1}$$

In order to generate a microwave signal, two optical signals with two different frequencies are combined. The combined signals are then sent to a photodector which detects the combined intensity of the two signals. The photodector measures the difference in the frequency, which is in the microwave range (on the order of MHz to GHz)[10]. The resultant microwave signal can be read by conventional electronics for the purpose of time keeping.

All clocks, including atomic clocks, drift over time as a result of frequency instability (changes in frequency due to thermal noise and mechanical shifts [12]); therefore, the oscillator in the optical atomic clock is designed to reduce this instability. The improvements in stability are useful only if they can propagate through the entire system. Therefore, the stability of the microwave output is also dependent on the individual frequency stability of the frequency comb itself. For this reason, the optical frequency comb must not drift in order to preserve the stability of the atomic reference. A frequency comb can be "locked" in place by locking individual comb lines to stable references. Since there are three unknowns in equation 1.1, two of the values must be fixed to order to determine the last value. In the case of the optical atomic clock, a comb line is locked to the ultra stable oscillator laser. Equation 1.2 shows the comb equation when the local oscillator is locked to a particular comb line.

$$f_{LO} = n f_{rep} + f_{CEO} \tag{1.2}$$

The comb must also be locked at f_{CEO} so that the relative frequency of the entire comb does not drift over time. Frequency division, the method for down converting from optical frequencies to microwave frequencies, occurs by dividing the difference between the local oscillator frequency and the offset frequency by the mode number selected [13]. The comb line that the local oscillator must be locked to is determined by the comb line that is closest to the optical frequency reference. In the case of the optical atomic clock system this would

16

be the comb line nearest to the oscillator frequency. Fixing one line to the local oscillator and locking the f$_{CEO}$ will stabilize the repetition rate. Equation 1.3 shows this relationship.

$$f_{rep} = (f_{LO} - f_{CEO})/n \qquad (1.3)$$

The frequency stability of the optical atomic clock's oscillator needs to be propagated through the optical frequency comb in order to be utilized by the microwave detector. The microwave stability is dependent on the stability of f$_{rep}$, since f$_{rep}$ is the clock output. The repetition rate's frequency stability is determined by the frequency stability of the clock's oscillator (δf$_{LO}$) and the frequency stability of f$_{CEO}$. The stability of the repetition rate is dominated by f$_{CEO}$ since the oscillator is ultra-stable. The frequency stability of the repetition rate is characterized by equation 1.4.

$$\delta f_{rep} = (\delta f_{LO} - \delta f_{CEO})/n \qquad (1.4)$$

In order to achieve a stable comb, the optical frequency comb used for APHI requires a series of locks for operation. The first locks the offset frequency of the comb using a technique called f-2f self-referencing and second harmonic generation (described in Chapter 3). The second lock stabilizes the comb to the optical atomic clock's laser reference. These locks fix the low frequency and the high frequency ends of the comb in order to prevent drift. Chapter 2 and Chapter 3 of this thesis describe experiments that contribute to the f$_{CEO}$ stabilization derived from f-2f.

1.2.1 Radio Frequency Noise Floor Comparisons

An optical frequency comb acts as an interface between optical frequencies and radio frequencies (RF). Therefore, the output of the optical frequency comb (and the optical atomic clock system) is an RF signal that must be characterized. This RF signal will often be the repetition rate of the optical frequency comb or the carrier envelope offset frequency. The stability of the clock will be evaluated at the output; therefore, understanding the accuracy of this measurement is essential in clock development. Each RF instrument's noise floors and

the corresponding signal-to-noise ratio of a measurement are different; therefore, it is important to evaluate the instrument's noise noise in order to improve measurement accuracy. In addition, the data capturing parameters of the measurement instrument (e.g. bandwidth, resolution, memory) determine which devices are best suited to record a particular measurement. With a variety of instruments to choose from, it is critical to know when each instrument should be used. Chapter 4 will discuss the methods and results of this study and how they can apply to optical frequency comb development.

1.3   Outline

This thesis is organized as follows: Chapter 2 will focus on the design and construction of the a lab-built 2μm laser that serves as an input to second harmonic devices. Chapter 3 will focus on the second harmonic generation required for the locking of the f_{CEO} using Periodically Poled Lithium Niobate (PPLN) second harmonic devices. Chapter 4 will focus on the analysis of RF instruments in lab and their applicability to optical frequency combs and optical atomic clock experiments. Finally, Chapter 5 will conclude and summarize the work.

2. LAB-BUILT 2 μm FIBER LASER

2.1 Motivation

As described in the introduction, in order to stabilize the frequency comb the f_{CEO} must be locked using f-2f self-referencing (see Chapter 3). Due to the characteristics of the devices generating the comb, this lock requires light near 1 μm, which can be created using a second harmonic generation device and a 2 μm light source. Periodically poled lithium niobate (PPLN) devices (further described in Chapter 3) are second harmonic devices capable of generating 1 μm light, and a 2 μm laser is needed to generate light near 2 μm in order to test and utilize these devices. The 2 μm laser described in this chapter was built in the lab and is not commercially available. The advantage of building a laser is the cost was be minimized by leveraging equipment and parts already present in the lab. In addition, the manufacturing time was reduced since only a few less complicated components needed to be ordered. While building our own laser did reduce system complexity and cost, it did possess a limited tunable wavelength and inconsistent power output values. This chapter will describe the setup, results, and potential future improvements of this laser.

2.2 Basic Laser Theory

A laser generally consists of three parts: a pump source, a gain medium, and a feedback network. The pump source provides the initial excitation in the lasing medium by transferring energy to atoms in the gain medium so they can move to their excited states. An in-exhaustive list of possible pump sources include flash lamps, chemical reactions, radiation, heat or another laser [14]. The gain medium consists of a material that produces photons as electrons descend from higher energy levels to lower energy levels. The distance between the energy levels determines the resultant wavelength [14]. Finally, the feedback loop causes the emitted photons to travel back and forth through the cavity, which facilitates further photon emission. The feedback loop must be designed so that the gain exceeds the loss. If the losses of the feedback system exceed the gain, the intensity of the beam will not increase and the system will not lase [11].
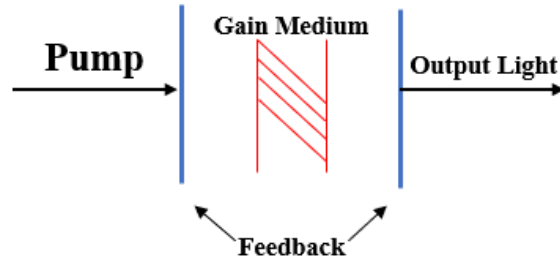
Figure 2.1. Basic laser configuration including a pump source, gain medium, and feedback system

Another important consideration for the lab-built 2 μm laser is the laser gain competition phenomenon. This is particularly important since the 2 μm laser must be tunable in order to match the conversion wavelength of the second harmonic devices. In the case of a broadened laser transition, there exists a band where lasing can occur, and this band can encompass many wavelengths depending on the size of the region. However, only the wavelength with the highest gain to loss ratio will emit from the laser [14]. As the properties of the cavity and/or the pumping power change (as is the case with a tunable laser), the modes that possess the largest gain to loss ratio can change. As a result, multiple wavelengths can compete for gain within the medium, leading to a reduction in the maximum gain of the desired wavelength and a reduction in its output power. In a fiber laser as considered here, different modes have different threshold powers; therefore, some of the modes may not appear until a particular pump power is utilized. Gong, et al. explain that at lower threshold powers, only certain modes will dominate the output gain. However, as the pump power exceeds the threshold of higher order modes, the higher order modes will make up a significant proportion of the output power [15]. The consequences of laser gain competition will end up limiting the tunable wavelength range of the lab-built laser.

2.3   Setup

The configuration for the laser setup was inspired by Geng's 2 μm ring laser in [16]. The schematic for the laser set up is shown in Figure 2.2. Figure 2.3 is a photograph of the labo-

ratory set up. A 1560 nm tunable laser serves as the pump source for the laser. The thulium doped fiber is the gain medium in this laser setup, and the ring structure of the laser is the feedback loop. Thulium was chosen as the gain medium for this laser because it possesses an emission spectrum around 1700 nm – 2100 nm [17], which will enable lasing near 2000 nm. The pump laser generates a 1560 nm signal which runs through a PriTel erbium doped optical fiber amplifier (EDFA) to the 1550 nm port of a wavelength-division multiplexer (WDM). The common port of the WDM sends the light through the Tm- doped fiber and an Agiltron manual etalon-based fiber optic tunable filter (with a specified bandwidth of 1 nm and a tunable range of 100 nm centered at 2000 nm). The laser is setup in a loop structure with a 70-30 coupler (rated as 75-25 at 2000nm) used to extract the output. The output is extracted using the 25 percent end, while the 75 percent end keeps the light within the loop. Finally, the light passes through a second WDM in order to further attenuate the residual 1560 nm pump light. The components are connected using fiber connectors as opposed to splicing the fibers together. The final laser assembly (without the pump laser and amplifier) was mounted to a metal prototype board for transportation between laboratories and experiments.

2.4   Results

The laser design as specified above can produce light from 1938 nm - 1992 nm. Figure 2.6 shows a summary of the efficiency of the laser for various output wavelengths. The efficiency of the laser (as a function of the pump power read from the EDFA) diminishes as the wavelength of the output is increased. This is due to the threshold pump power required to lase at larger wavelengths increasing and gain saturation of the Tm doped fiber limiting the output power. A result of the gain medium's saturation, the maximum output power for the laser is approximately 0 dB at 1980 nm. In addition, as the wavelength of the output light increases, the corresponding output power decreases. As a result, the output power at a particular pump power will vary for each wavelength setting. In Geng's setup, the most efficient wavelengths were found in the center of the 200 nm tunablilty range (approximately
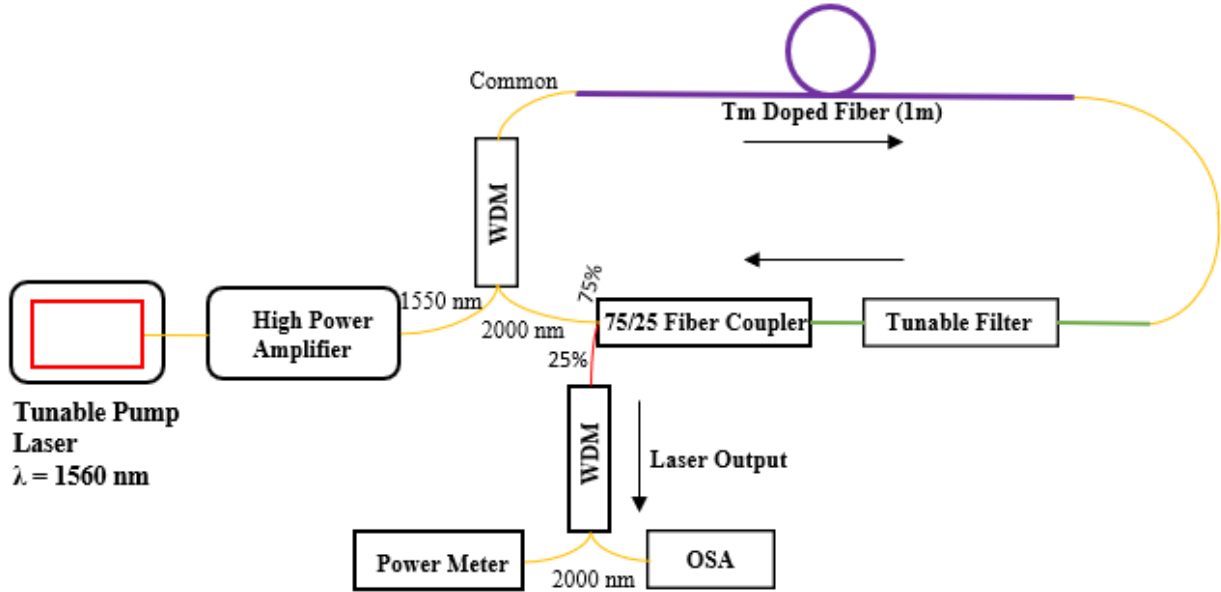
Figure 2.2. High level diagram for the 2 μm Laser. WDM: wavelength-division multiplexers (with 1550nm/2000nm ports). OSA: optical spectrum analyzer (1200nm – 2000nm).
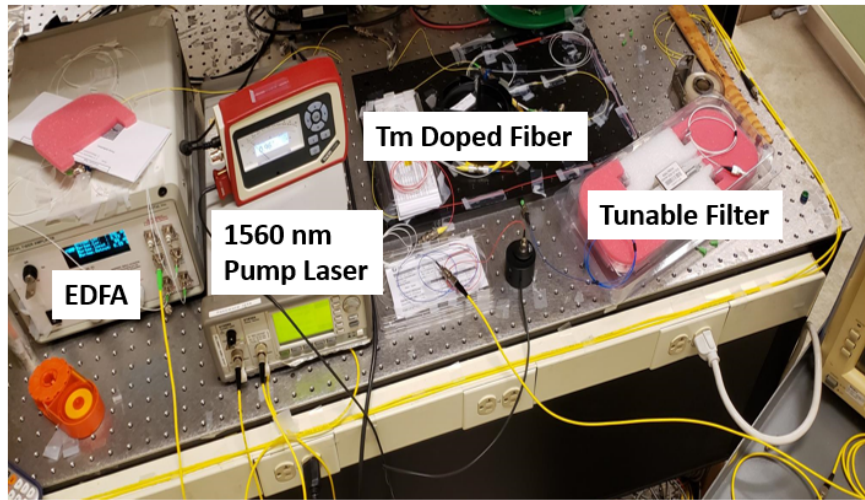
Figure 2.3. Laboratory setup of the 2 μm laser

1900-1960 nm) [16], whereas for this laser, the best efficiencies occurred at the shortest wavelengths near 1940 nm. Around $\sim$ 1940 nm are the shortest wavelengths due to the minimum wavelength limitation of the tunable filter (as illustrated in figure 2.8).
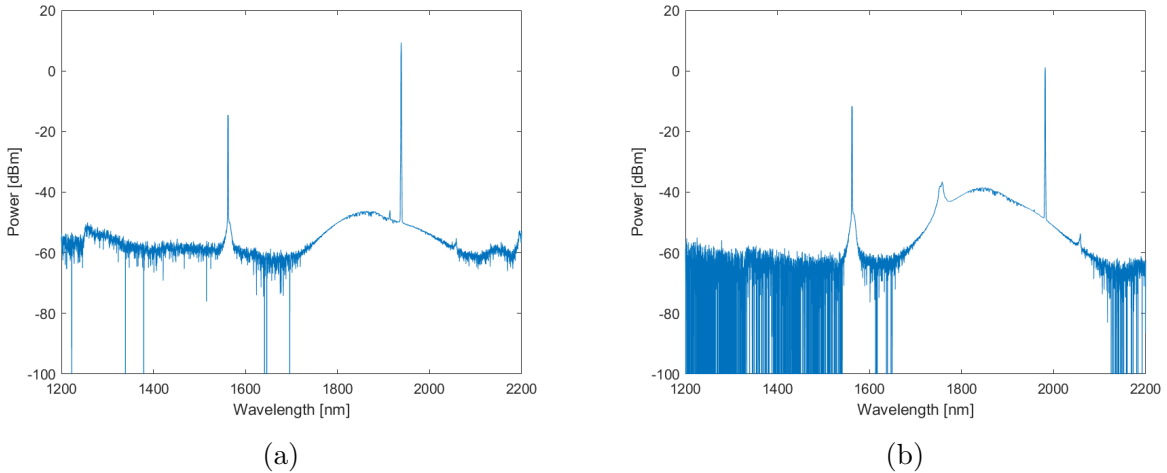
Figure 2.4. An example 2 μm laser spectra taken on the 2 μm OSA. a) shows the minimum tunable wavelength of 1938 nm. b) shows the spectrum when the laser is tuned to 1982 nm.

Figure 2.4 shows two examples of the laser's output spectrum taken on the 2 μm OSA which characterizes the minimum and maximum wavelengths of the tunable laser. The image in figure 2.4(a) shows the minimum wavelength of approximately 1938 nm and a power of 9.37 dBm. The residual pump at 1560 nm has a power of -14.55 dBm. As read from the EDFA (as opposed to measuring the EDFA output power using a power meter), the laser was pumped at 1.25 W. Similarly, in figure 2.4(b), a spectrum of 1982 nm light is shown. The output power at this wavelength was approximately 1 dBm, and the residual pump at 1560 nm had a power of -11 dBm. The pump power setting on the EDFA was 1.5 W.

The laser linewidth is determined at the full width of the spectrum at half maximum (FWHM) [14] which is the -3 dB point from the maximum value of the laser line. When operating at approximately 1940 nm, the linewidth of the lab-built laser at FWHM is approximately 0.07 nm or ~4 GHz. This measurement was made with the smallest resolution setting on the OSA (0.05 nm). Since, 0.07 nm and 0.05 nm are close in value, the measured linewidth may be broadened by the resolution filter inside of the OSA. Linewidths that are more fine than ~4 GHz cannot be accurately measured using the OSA at this wavelength due to its resolution limit. Figure 2.5(a) shows an example of the peak at 1940 nm. Figure

2.5(b) shows the peak wavelength of the 2 μm laser during 7 minutes of operation. The laser wavelength deviates only 0.02 nm which is within the resolution of the OSA.

(a)   (b)
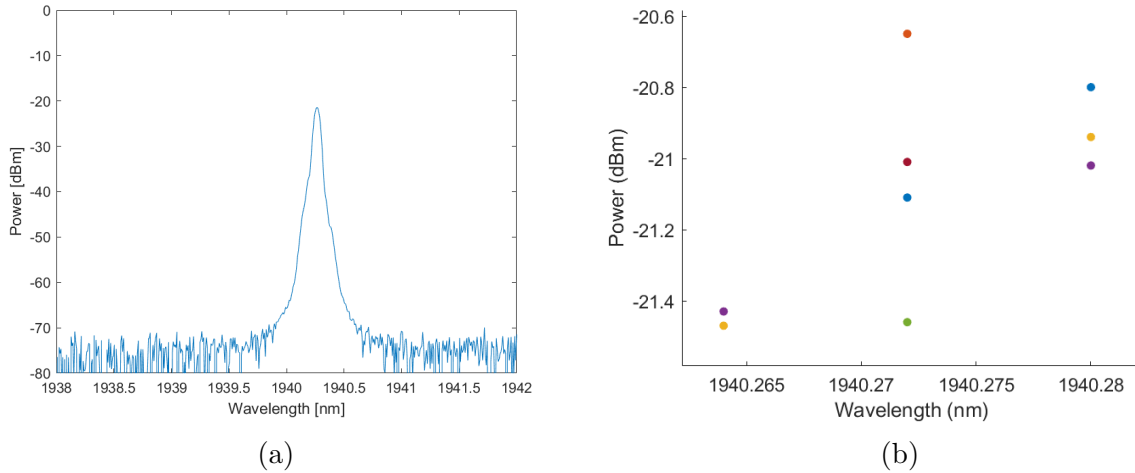
Figure 2.5. (a) 1940 nm peak of 2 μm laser output. OSA Resolution: 0.05 nm (b) an example of wavelength drift taken over a 7 minute span of operation.

Figure 2.6 highlights the inconsistency in the output power as the power fluctuates over time even if the wavelength remains constant. This power fluctuation was on the order of milliwatts at the output. This is a significant fluctuation because the total output power is on the order of tens of milliwatts. Therefore, the powers and efficiencies displayed are estimations determined by when the sample was taken. While the power fluctuates by a few dB over time, the wavelength of the output only drifts 0.1 nm as read by the OSA (figure 2.5 (b)).

While the original design goal of the laser was to operate at wavelengths near 2000 nm, a lasing phenomenon occurs that prevents this specific design from reaching that goal. After ~1982 nm, the system produces two different wavelengths of light, ~1760 nm and ~1992 nm. Both of these wavelengths occur within thulium's emission spectrum [17]. The two wavelengths compete for gain from the Tm-doped fiber, which limits the possible output power of the desired wavelength. As shown in Figure 2.6, the threshold power for longer wavelengths increases, and the lasing at ~ 1760 nm occurs at the same threshold value power as the 1992 nm light. On occasion, when the laser is operated, it is possible to operate above 1985 nm

24

2 µm Laser Efficiency with 1m of Tm Doped Fiber at Various Output Wavelengths
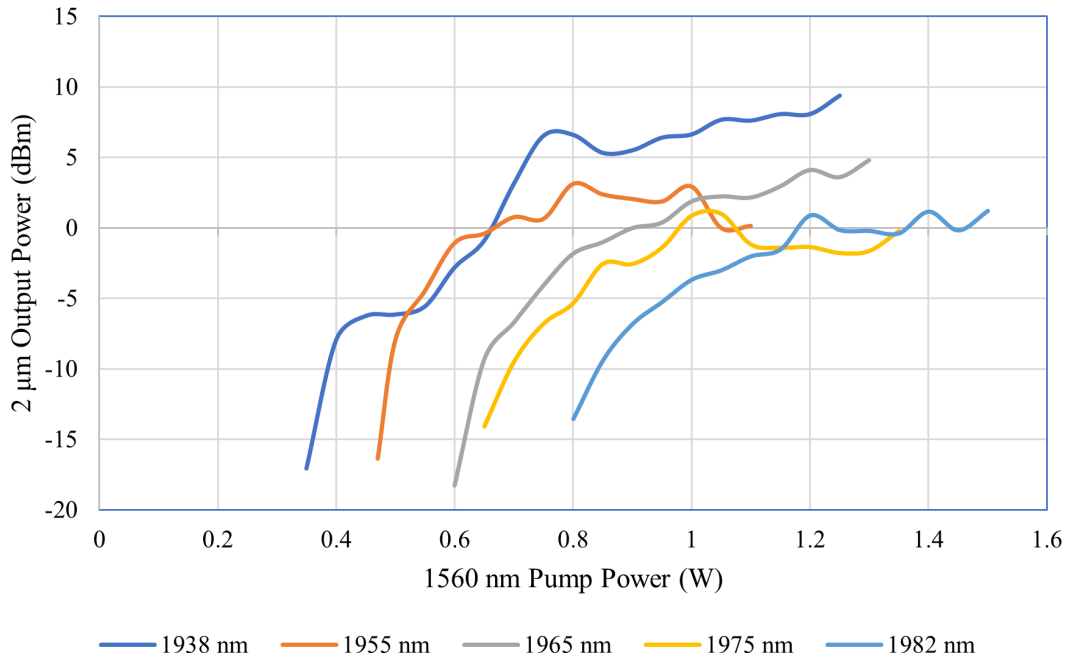
Figure 2.6. Efficiency of 2μm laser using 1 meter of TM doped fiber at various output wavelengths

without the presence of the extra lasing line; however, gain saturation and mode competition within the fiber laser prevent the laser from reaching wavelengths beyond this limit. Figure 2.7 shows the output spectrum approaching the maximum wavelength of the laser. In the case of Figure 2.7, the maximum wavelength is near 1992 nm, and the additional lasing around 1760 nm is also present. The lasing at 1760 nm is not filtered by the Agiltron tunable filter as shown by the calibration experiment conducted with the MENLO optical comb (see figure 2.8). The MENLO comb is a commercially available octave spanning frequency comb. In this calibration experiment, the MENLO comb, with an operational wavelength range of 1700 nm - 2200 nm, served as the input to the tunable filter. The filter was then adjusted from its minimum wavelength to its maximum wavelength in order to evaluate the tunabilty range of filter. Figure 2.8 shows the results of this calibration experiment using the Agiltron filter where the range is 93.8 nm from 1938.5 nm to 2032.3 nm ($\sim$6.2 nm shorter

than the specified 100 nm tunability range). Figure 2.8(a) displays the minimum of the filter passband and figure 2.8(b) shows the maximum value of the passband.
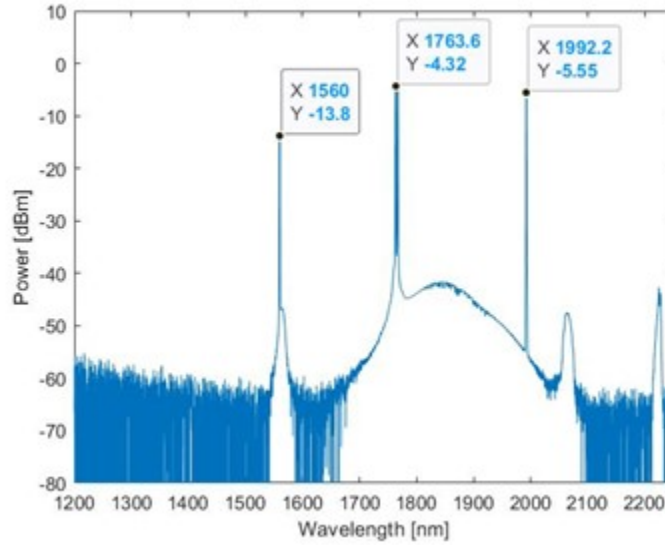
Figure 2.7. Maximum wavelength of 2μm laser exhibiting additional lasing at 1763 nm. The figure also shows the residual pump power at 1560 nm and the maximum output wavelength of 1992 nm.
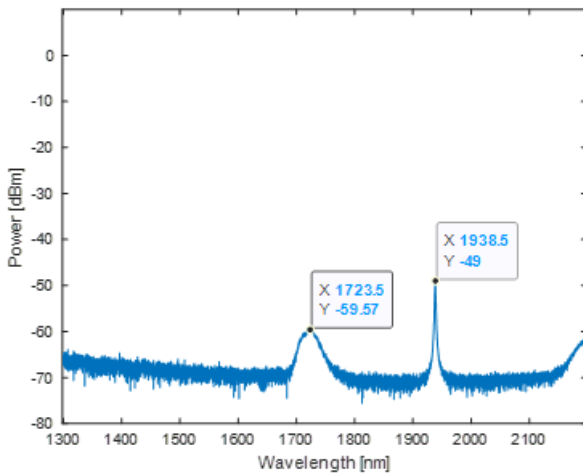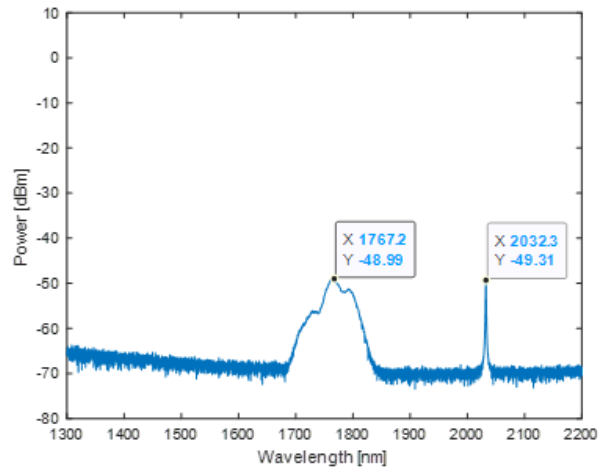
Figure 2.8. Tunable filter calibration using MENLO Comb and 95-5 fiber coupler. a) shows the minimum wavelength of the tunable filter pass band. b) shows the maximum wavelength of the tunable filter pass band.

When operating near the maximum wavelength of the laser and as the pump power is increased, the additional power contributes to the 1760 nm signal; therefore, increasing the pump power beyond 1.5W does not increase the operable wavelength of the laser nor the output power of the 2 μm light. After evaluation of the laser using 1 meter of Tm doped fiber, a second test was conducted using 2 meters of Tm-doped fiber. Adding a second meter of Tm doped fiber did not significantly change the operational wavelengths of the laser. However, it did increase the threshold pump power for lasing and the unintended lasing shifted from ~1760 nm to ~1850 nm. Both 1760 nm and 1850 nm are within the emission range of Tm doped fiber [18]. By changing the properties of the gain medium, the laser line at ~1860 nm became the dominate mode. Since, the tunable wavelength range and the 2 μm output powers were not improved by the additional meter of Tm-doped fiber, the final design of the laser included only 1 meter of fiber to reduce the threshold power that needed to be provided by the EDFA.

The current design for the ring laser does not contain a polarization controller which creates two separate challenges. The first challenge is the 2 μm output is affected by the orientation of the fiber in the system. If the setup is adjusted or moved then the output power of the laser will vary drastically (on the order of a few milliwatts). At 2 μm the polarization of the light is affected by the size of the fiber loops and their orientation. This is one of the causes of the power fluctuations displayed in figure 2.6. The second challenge is the output power of the laser fluctuates by a few milliwatts as the polarization changes within the system (another phenomenon that explains the multiple dB variation in the output power values shown in figure 2.6). If the laser output power needs to remain precise, a polarization controller would need to be added to stabilize the output power. In addition, in order to mitigate the gain competition with the extra mode, an additional filter needs to be implemented. This filter would need to attenuate the lasing that occurs at the 176 0nm since the Agilitron tunable filter passes this wavelength. Despite, the limited wavelength and power fluctuations, the 2 μm laser served as a valuable input to begin the characterization of the PPLN chips. Therefore, it was a valuable initial classification tool for the APHI project.

3. PERIODICALLY POLED LITHIUM NIOBATE

3.1 Motivation

As discussed in the introduction frequency locks are required to stabilize the frequency comb used in the APHI project. One of the required locks requires f-2f self-referencing in order to lock the f_{CEO}. F-2f requires the frequency of a comb line be doubled to twice the frequency. The required wavelength is determined by the f_{CEO} of a viable comb line pair because there must be a high frequency comb line around this wavelength in order to lock. This wavelength of light is created by using second harmonic generation (SHG) and periodically poled lithium niobate (PPLN) chips. Dr. Kaiyi Wu tested viable comb line pairs and determined that an SHG wavelength of about 980 nm is required from the PPLN chips to complete the self-referencing. The goal of the experiment was to characterize PPLN chips from the commercial vendor SRICO, Inc. to find viable devices for this lock. The documentation from SRICO contained limited information on the center frequencies and operating conditions of their devices; therefore, this experiment was used to explore the center frequencies and conversion efficiencies of many of these devices.

3.2 Theory

3.2.1 F-2F Self-Referencing

The f_{CEO} lock is achieved using the F-2F self-referencing technique. In this technique, the high frequency comb lines are compared to the low frequency comb lines and the difference between the two is the carrier envelope offset frequency. In order to achieve this measurement the low frequency comb line is doubled and then optically heterodyned with the comb line at twice the frequency. Since, the low frequency comb line must be doubled, this can only occur with an octave spanning comb (where there is at least a factor of 2 between the low frequency and high frequency lines). The frequency doubling is achieved by using a second order non-linear device (described below) to achieve the frequency doubling. The two comb lines are optically heterodyned then they are sent to a photodetector, which detects the intensity of the heterodyne, and determines the frequency difference in the two signals. The

difference is an RF signal on the order of 10s of GHz. The resultant RF signal is the f_{CEO}[19]. Equation 3.1 illustrates the optical frequency comb equation for the frequency doubled comb line [19]:

$$f_{2n} = 2nf_{rep} + f_{CEO} \tag{3.1}$$

By taking the difference of the frequency doubled comb line and the comb line at $2f_n$, f_{CEO} can be determined [19], [20].

$$2f_n - f_{2n} = f_{CEO} \tag{3.2}$$

F-2F self referencing is the technique that connects the PPLN device experiments described in this chapter (and the 2 μm laser in Chapter 2) to the optical frequency comb and therefore, the optical atomic clock.

3.2.2 Non-Linear Optics

In order to describe the operation of PPLN devices, it is necessary to give a very brief overview of relevant non-linear processes. In optics there are both linear and non-linear materials and their classification is determined by their response to an input electric field. In a linear material, the frequency of the output light does not change. However, in a non-linear material, the output light may contain new frequencies.

The polarization due to an interaction with a material can be described by a Taylor series as follows: [21]:

$$\tilde{P}(t) = \chi^{(1)}\tilde{E}(t) + \chi^{(2)}\tilde{E}^2(t) + \chi^{(3)}\tilde{E}^3(t)...\chi^{(n)}\tilde{E}^n(t) \tag{3.3}$$

PPLN devices are a second order material, which means that their response to input light is $\sim E^2$ as shown by the polarization equation highlighted above. The second order phenomenon of interest to our experiments, that occurs in PPLN devices, is SHG. In second harmonic generation, the material generates two output frequencies: one at ω and another at 2ω.

If a wave is described by a basic solution to the wave equation:

$$\tilde{E}(t) = E\mathrm{e}^{-\mathrm{j}\omega t} + E^*\mathrm{e}^{+\mathrm{j}\omega t} \tag{3.4}$$

and that wave is passed through a second order material, then the polarization equation can be written as [21]:

$$\tilde{P}^{(2)}(t) = 2\chi^{(2)}EE^* + \chi^{(2)}E^2\mathrm{e}^{-2\mathrm{j}\omega t} \tag{3.5}$$

Since equation 3.3 is a Taylor series expansion, substituting equation 3.4 into 3.3 will result in 3rd order, 4th order, etc. effects. Each of these values will have their own χ value for a particular material, indicating the strength of the response. In practice devices have responses of multiple orders. The efficiency of a second-harmonic device is described by [22]:

$$\eta_{2\omega} = \frac{P_{2\omega}}{P_\omega^2} \tag{3.6}$$

where $P_{2\omega}$ is the power of the second harmonic light and P_ω is the power of the input light.

3.2.3 Periodically Poled Lithium Niobate

Lithium Niobate ($LiNbO_3$) is a synthetic salt. Its non-linear properties are described by its non-linear susceptibility. The non-linear susceptibility is characterized by a crystal symmetry and orientation [21]. PPLN devices possess a second order non-linearity and a phase matching condition that allow them to generate second harmonic light. For this reason, they are employed for the f-2f self-referencing scheme.

3.3 Experimental Setup

In our lab there are seven chips each with 36 PPLN devices made by SRICO. Each of the devices is a waveguide that facilitates SHG. The chips are not fiber coupled; therefore, coupling onto the devices needed to be completed manually. The chip was mounted on a stage that could adjust the tilt of the chip in addition to moving the entire chip from one device to the next. The output fiber was fastened on a stage with three axis tuning and the

input was anchored on a stage with three axis tuning in addition to angular tuning. Using a microscope and a microscope illumination source, the fibers could be aligned in order to minimize the coupling loss onto and off of the chip. The PPLN was pumped using the output of the 2000 nm laser (Chapter 2), the broadband amplified spontaneous emission profile of a Cybel thulium doped fiber Amplifier (TDFA), or a commercial 2 μm laser from Sacher Lasertechnik. A setup for the schematic is depicted in Figure 3.1. Figure 3.2 is a photo of the laboratory setup.
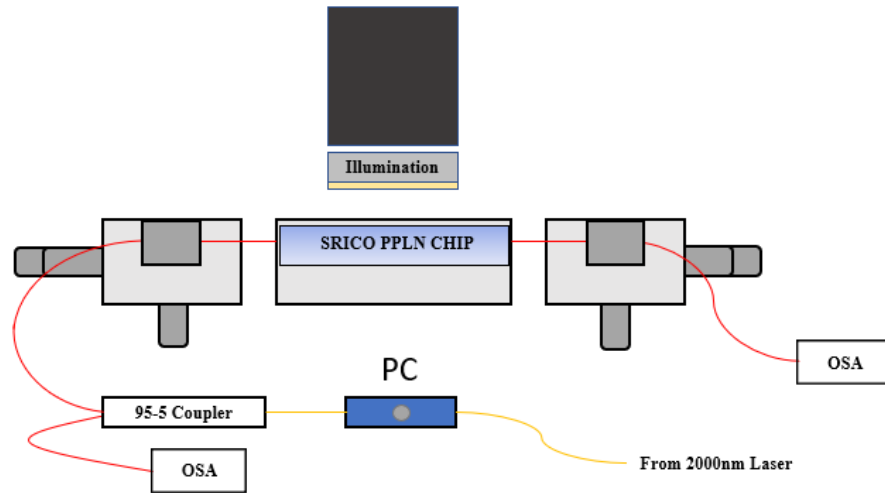
Figure 3.1. PPLN testing set up. The setup includes a OptixCam Summit series microscope in order to couple the fibers to the devices. The OSA on the 5% end of the 95-5 coupler was used to monitor the wavelength input laser wavelength. The OSA after the chip was used to measure the SHG light.

Figure 3.3 shows the layout of the PPLN waveguides on the chip. The waveguides are spaced in groups of 4 down the chip with device 1 appearing at the top of the device and device 36 on the bottom.
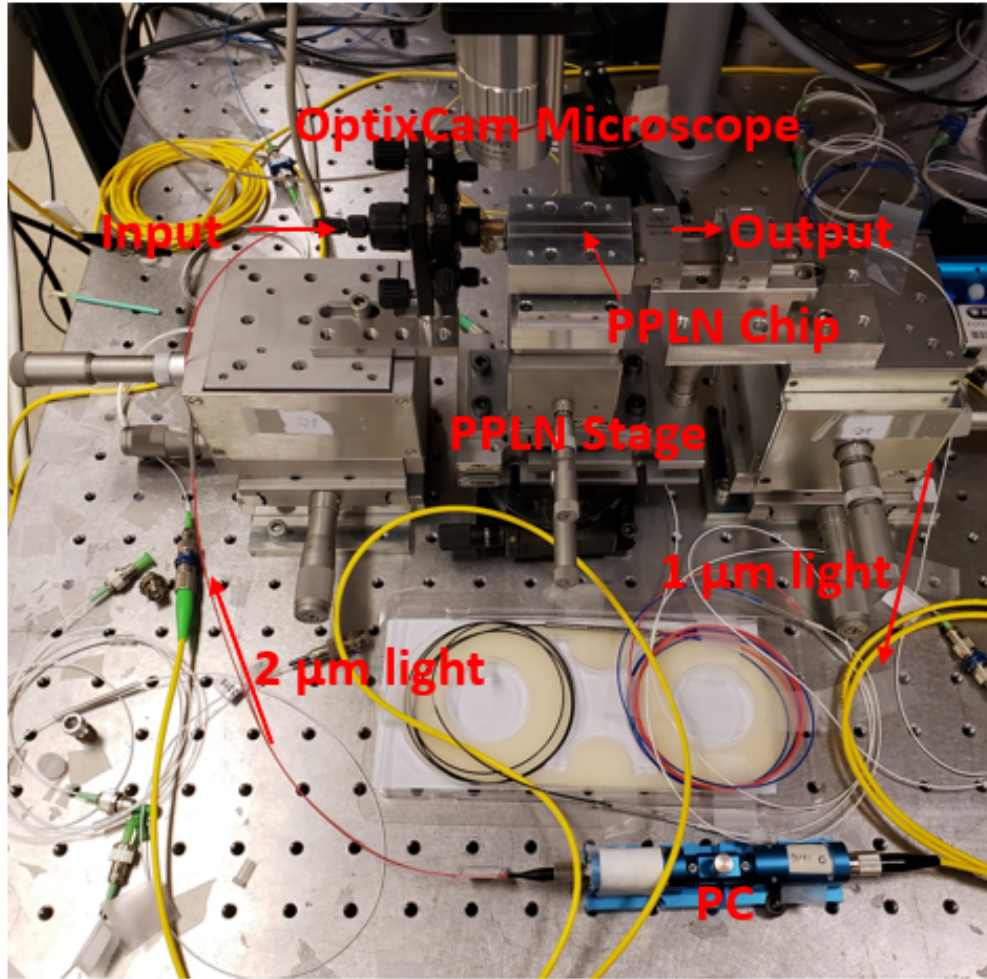
Figure 3.2. Photo of the PPLN setup. The 2 μm light moves passes through a polarization controller (PC) before being coupled onto the chip. The output fiber is coupled to the output of the device to collect the 1 μm light.

When coupling to lithium niobate chips, there is a risk of scratching the waveguides with the fiber. In order to mitigate this risk, yet move the fiber close to the device, glycerin was applied to the fiber tip to act as a barrier between the fiber tip and the waveguide. The laser light will diverge from the coupling fiber, causing additional loss. In order to reduce this loss, the coupling fiber must be very close to or touching the waveguide. In addition, the glycerin serves as an index matching gel to reduce the coupling loss. Figure 3.4 shows the coupling of the fiber to the output of a device using the OptixCam microscope.
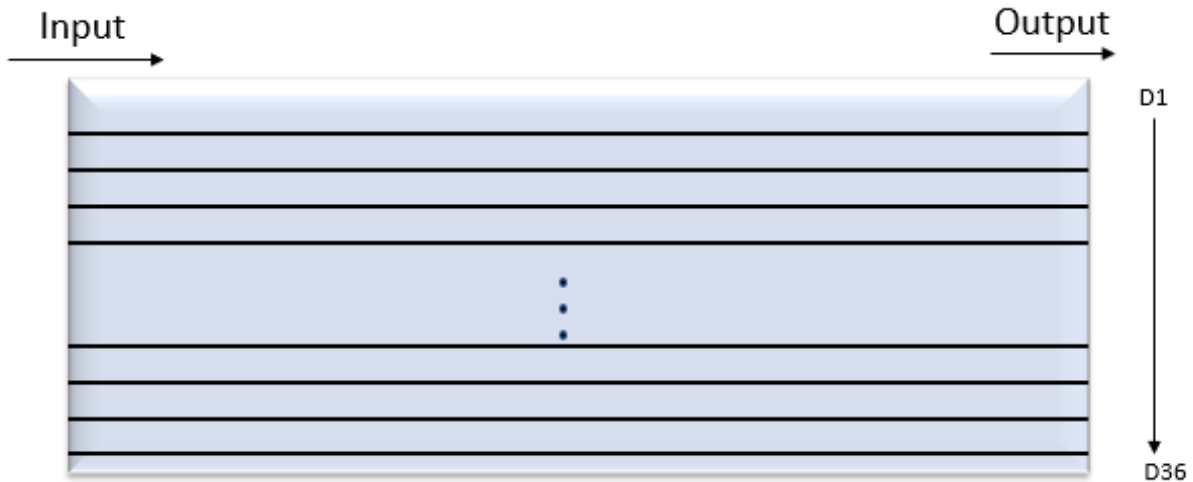
Figure 3.3. Graphic of the layout of PPLN waveguides on a chip based on the documentation from SRICO, Inc.
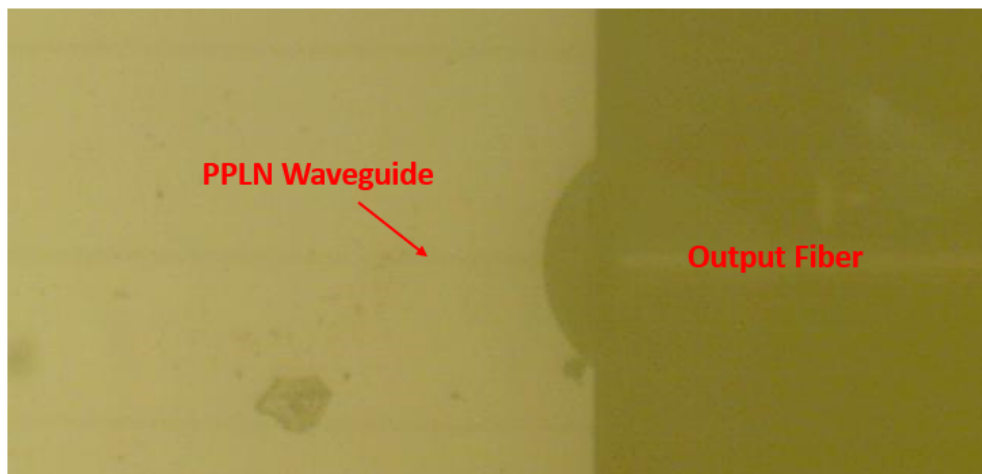
Figure 3.4. The output fiber coupled to a PPLN device viewed using the OptixCam microscope. The fiber has a layer of glycerin applied.

3.4 Methods and Results

The PPLN devices were tested in order to determine the center frequencies of the devices and evaluate their efficiencies. A few devices on each chip were assessed in order to generally characterize the chip. In order to meet this goal, three different inputs were used. The first was the lab-built laser explained in Chapter 2. This laser possessed enough input power to generate second harmonic light, but had a limited tuning range. The second input was

the amplified spontaneous emission profile of a thulium doped fiber amplifier (TDFA) which possessed a larger wavelength range, but a lower input power. Finally, some devices were tested using a commercial 2 μm laser from Sacher Lasertechnik, which possesses enough input power for second harmonic generation and a wider tunable range than the lab-built laser. Most of the SRICO devices have a waveguide width of 8 μm at the input and a waveguide width of 6 μm at the output. However, devices, 1, 13, and 25 on each chip possess a 8 μm output facet. The larger facet values were generally easier to couple because the 8 μm facets did not attenuate the 2 μm input as completely as the 6 μm outputs – leading to larger total power values on the output.

3.4.1   Lab Built 2 μm Laser and Thulium Doped Fiber Amplifier Inputs

As described in Chapter 2, the lab built 2 μm laser has a limited tuning range which means that only a particular range of center frequencies could be accessed using this laser. Some of the documented center wavelengths from SRICO, Inc. are outside of this tunable range; therefore, the performance of these devices were not assessed using the laser and a center wavelength could not be established for such devices. The lab-built laser's operational wavelength range is ∼1938 nm - ∼1985 nm which facilitates a second harmonic generation range between ∼968 nm and ∼992 nm.

In an effort to widen the input wavelength range, the broadband amplified spontaneous emission profile of a thulium doped fiber amplifier (TDFA) was used as the input. The gain profile extends from ∼1850 nm - 2000nm. Unfortunately, the gain profile of the TDFA (without an input) had a low spectral power density compared to the 2 μm laser which possesses up to a maximum 8 dBm of power at a singular wavelength. This meant that in a few cases the TDFA was able to generate second harmonic light outside of the lab built 2 μm laser wavelength range (a handful of devices with center wavelengths between 947 nm and 957 nm), but it did not have the required power for SHG on many devices. This was verified by using the TDFA as the input to chip C7 with an operational range of ∼ 978-980

nm. The TDFA was not able to generate SHG light on this chip whereas the lab built 2 μm laser was able to produce SHG on the same devices.

For most of the chips, only a few devices were tested in order to generally characterize the chips. Since center wavelengths were different down the chip, various devices located at different parts of the chips were tested. Often this would indicate whether or not the chip possessed devices in the testable range of the 2 μm laser or the TDFA. When using the lab built 2 μ m laser, the coupling loss was determine by measuring the power going onto the chip and the power coming off the chip. This power reflected the total power including the residual 1560 nm pump power, the 2 μm laser output, and the second harmonic light. The coupling loss was approximately 10 dB for the better coupled devices. However, it was not a precise calculation as the multiple dB power fluctuations from the laser, as described in Chapter 2, prevented a exact power measurement at any particular point in time.

When determining the overall conversion efficiency, the loss due to the coupling is included in the calculation (meaning that it is not factored out when determining the conversion efficiency). The overall efficiency was determined by comparing the power of the input $\sim$2μm laser light and the output SHG light according to equation 3.6. When performing this calculation $P_{2\omega}$ is power of the second harmonic wavelength read on the OSA and P_{ω} is the power of the $\sim$ 2μm light input also read from the OSA.

The device selected for the optical frequency comb experiments is Device 13 from Chip C6 since it had one of the higher SHG powers of the tested devices. In addition, this device has a measured center wavelength of $\sim$978 nm, which is in the range of the required wavelength for f-2f. For this reason, this device was chosen for much of the PPLN analysis, since its operation is relevant to the APHI project, optical frequency combs, and optical atomic clocks. Using the 2 μm laser the overall efficiency was approximately 0.02317/W. This efficiency calculation is approximate due to the fluctuation in the input power as stated before.

Figure 3.5(a) shows the input spectrum to device C6D13 sampled through the 5 percent end of a 95-5 coupler and figure 3.5(b) shows output second harmonic light. With an approximate input power of 2 mW (total input power read using a power meter) and an output power of $400\mu W$ (the total output power also read by the power meter), the coupling loss is approximately 7 dB.

(a)

(b)
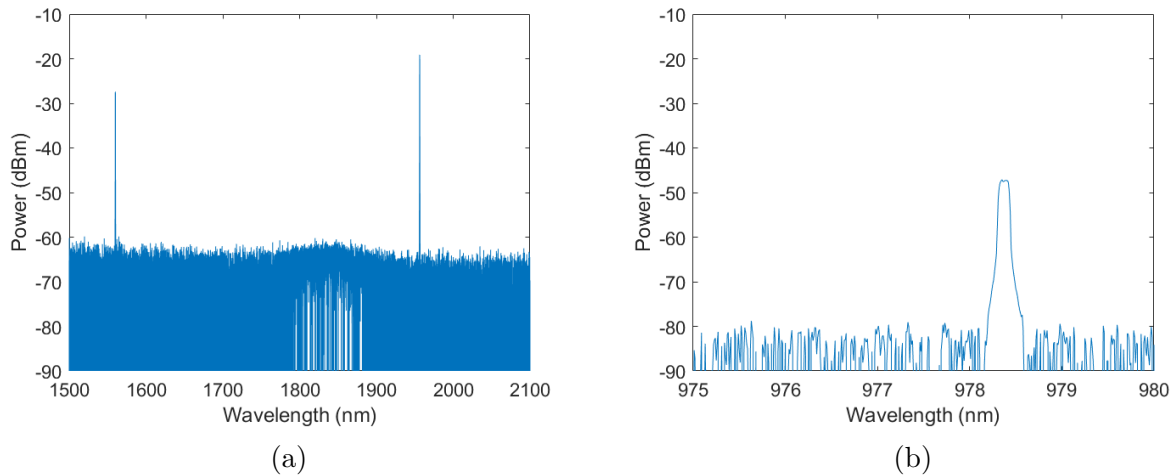
Figure 3.5. (a) the 2 μm input (b) the corresponding second harmonic generation peak of C6D13

Furthermore, since PPLN is thermally dependent, adjusting the temperature of the stage will shift the operational wavelength the devices. If a particular center wavelength was required, the chip could be heated, using a temperature controller, to adjust the center wavelength. The specification from SRICO for the thermal tuning is 0.11 nm/°C. Figure 3.6 shows an example of thermal tuning applied to C6D13. On this device, adjusting the temperature affected the center wavelength about 7 times more than the specification (0.75 nm/°C compared to 0.11 nm/°C).

While the 2 μm laser possessed a limited tunable range and power fluctuations, it did allow for an initial characterization and selection of PPLN devices for the APHI project. Table 3.1 provides a brief summary of the wavelength ranges and SHG outputs powers of some of the devices tested using the lab-built laser. There were other chips and devices that

(a)	(b)
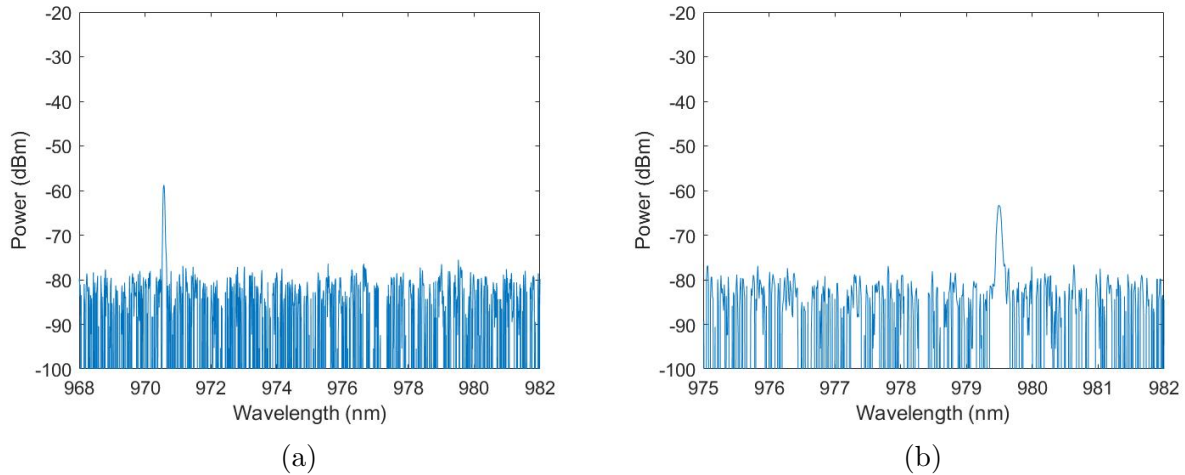
Figure 3.6. Thermal tuning performed on C6D13. (a) shows the SHG when the chips is heated to 28 °C. (b) shows the chip when heated to 40 °C. The wavelength shifts by 9 nm for a thermal tunability of 0.75 nm/°C.

were tested, but the center wavelengths were likely outside of the testable frequency range; therefore, they did not have a measurable SHG response. The data for chip C4 was acquired using the TDFA ASE profile. The tested devices on this chip (devices 1-4, 13-16, and 25-27) had a wavelength range between 943.45 nm and 957.88 nm. This same range of devices had SHG output powers in the range of -74 dBm - -62 dBm.

Table 3.1. Summary of PPLN devices tested using lab-built 2 μm laser

Device Range	SHG Wavelength Range (nm)	2 μm Input Power Range (dBm)	SHG Output Power Range (dBm)	Overall Efficiency Range (/W)
Chip C7 Devices 1-14	977.448 - 982.77	-8.91 - -0.96	-72.65 - -50.57	0.00064 - 0.112
Chip C6 Devices 1-9, 13-25	969.32 - 978.38	-4 - 1.07	-75.68 - -37.45	0.000024 - 0.243
Chip C5 Devices 1, 5, 13-16, 25-28	968.84 - 971.23	0.36 - 5.02	-72.03 - -42.6	0.00002 - 0.008

In table 3.1 the largest 2 μm input power values do not necessarily correspond to the highest SHG output powers. Similarly, the largest SHG output powers do not necessarily correspond to the best efficiency values. This is due to the time variance in the 2 μm laser power that causes a few dB discrepancy between the measured input power value and the actual power value at the time of the SHG power measurements. As a result, the overall efficiency ranges for these devices are only estimations because the measured SHG power may not correspond to the measured 2 μm laser input power. Due to these inaccuracies, retesting the devices with the commercial 2 μm laser provides a way to verify the efficiency values. Also in comparing the input power ranges of each of the chips, each chip was measured at a different point in the semester, so the 2 μm laser power was different due to its sensitivity to bending, orientation, pump power, etc. This is why the input power ranges between chip C7 and chip C5 vary by nearly 15 dB.

3.4.2   PPLN Testing using the Commercial 2 μm Laser

The Sacher Lasertechnik Tunable External Cavity Laser is a commercially available tunable laser with a tunable range of 1850 nm - 2000nm and a tested output power of $\sim$0 dBm at 1850 nm and $\sim$7 dBm at 1950 nm. The specified linewidth for the laser is on the order of $\sim$100 kHz. This commercial laser was used on chip 6 device 13 and chip 6 device 1 to reevaluate the efficiencies determined with the lab-built laser. Figure 3.7 shows a comparison of the SHG output power of device C6D13 using the built 2μm laser and the commercial 2μm laser. The efficiency using the Sacher laser improved the efficiency on this device to 0.0567/W compared to approximately 0.02317/W using the lab-built laser. The discrepancy in the linewidth shown in figure 3.7 can likely be attributed to the resolution setting of the OSA at the time of measurement. The Sacher laser plot was taken using the finest possible resolution on the OSA (0.01 nm), but the lab-built laser measurement may not have been.

Furthermore, figure 3.8 shows the range of second harmonic generation before the SHG power disappears into the noise floor of the OSA. The measurement was completed by sweeping the input wavelength by 0.5 nm until the SHG peaks were not detectable above the OSA
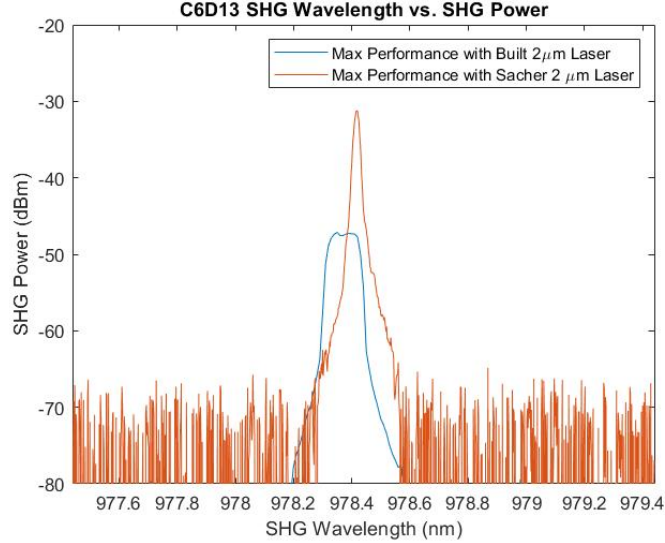
Figure 3.7. Comparison of Chip C6 Device 13 second harmonic generation using the built 2 μm laser and the Sacher 2 μm laser.

noise floor at ∼-65 dBm. Figure 3.9 displays the normalized SHG power of device C6D13. This plot was achieved by normalizing the SHG power values in figure 3.8. The normalized power should resemble a $sinc^2$ phase matching plot as shown in [23]; however, the data collected was hard to match to a fitting function since the SHG powers were not taken at fine enough wavelength intervals.

A similar approach was taken to establish the conversion bandwidth of the PPLN device. The conversion bandwidth is established at the FWHM value (or the -3 dB point). This was assessed by changing the input wavelength in increments of 0.1 nm, which corresponds to 0.05 nm shifts in the second harmonic wavelength. The 3 dB point of the device occurred at 978.206 nm and at 978.698 nm for C6D13 when measured with an OSA resolution of 0.01 nm. Therefore, the conversion bandwidth is ∼0.49 nm. SRICO specifies that the conversion bandwidth for their devices is 0.4 nm; therefore, the measured device conversion bandwidth is larger than the specified value. Due to the limited number of devices tested with the commercial laser, a conclusion on the conversion bandwidth on the lot of devices cannot be determined without testing the FWHM of more devices.

39
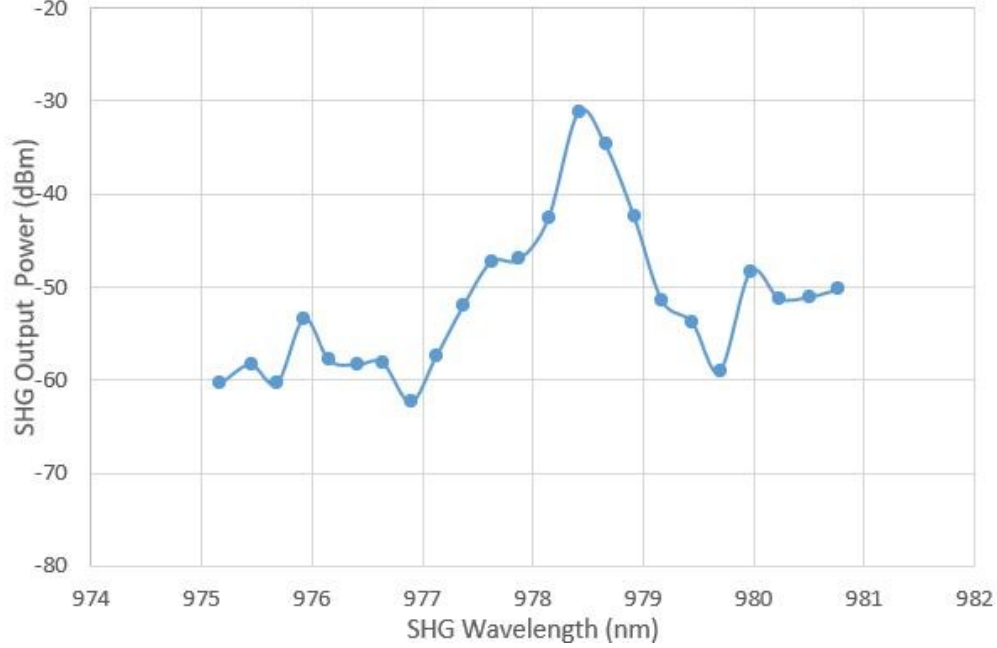
Figure 3.8. Range of SHG values on PPLN device C6D13

Device C6D1 on the same chip is specified by SRICO as the highest efficiency device. Therefore, this device was also examined using both 2 μm lasers. Unlike C6D13 the output power actually decreased when using the Sacher laser. As a result, there is a possibility that device C6D1 is damaged, reducing its efficiency. Also, since this device is specified by the manufacture to be the most efficient device, the results of the test with the Sacher laser do not match the specification as C6D13 outperformed C6D1 with this laser. In order to verify that the device is damaged, other devices on the chip will need to be tested to collect more data about the second harmonic response using the Sacher laser. The output power of this device using the built 2μm laser was ∼-37.45 dBm at 972.42 nm with ∼0 dBm of input power. Similar to the other devices, the data is approximate due to the multiple dB variation in the input laser power. The Sacher laser resulted in -38.66 dBm of SHG output at 973.702 nm with an input power of 5.38 dBm. Therefore, the measured efficiency of the device is 0.0114/W. Table 3.2 summarizes the results of the two devices that were tested using both the lab-built laser and the commercial Sacher laser. The lab-built input power,
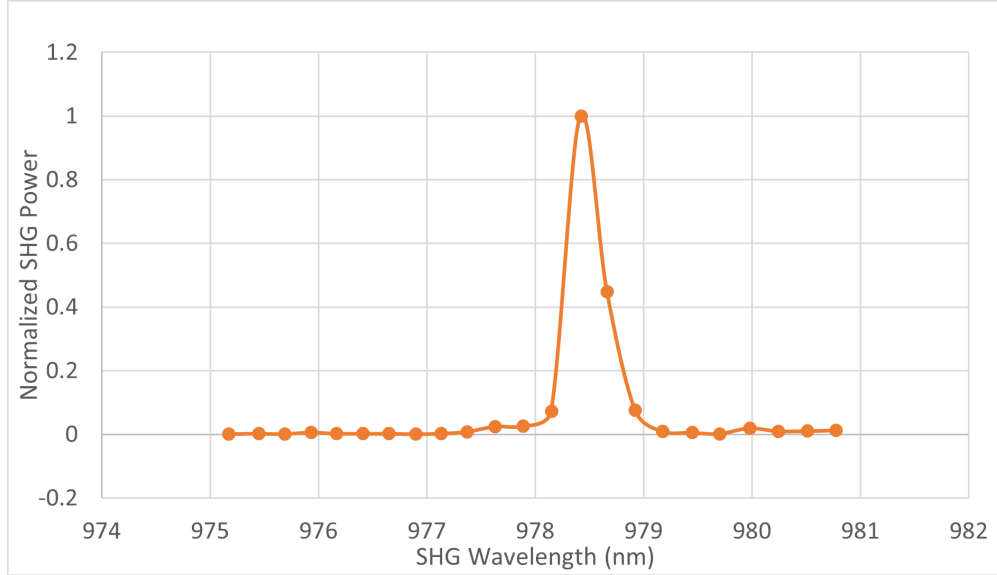
Figure 3.9. Normalized SHG power of device C6D13

the lab-built output SHG power and the lab-built efficiency are all approximations due to the multiple dB fluctuations in the lab-built laser output power.

Table 3.2. Summary of PPLN devices tested using lab-built 2 μm laser and commercial Sacher 2 μm laser

Device	Approximate SHG Wavelength (nm)	2 μm input (dBm) (Built/Comm)	SHG Output Power (dBm) (Built/Comm)	Overall Efficiency (/W) (Built/Comm)
C6D13	978	-0.6/5.63	-47.5/-31.2	0.0232/0.0567
C6D1	973.7	-0.65/5.38	-37.45/-38.7	0.243/0.0114

The calculated overall efficiency of the lab-built laser with device C6D1 is about 0.243/W which is likely too large of an efficiency for these devices even though C6D1 was specified as the most efficient device. With the output power of the lab-built laser fluctuating by a few dB it is likely that the SHG was at a peak and the input 2 μm light was near a trough when this measurement was taken. Based on equation 3.6, a small input power that does not correspond to a measured high SHG peak could hyper-inflate the overall efficiency. If the input power were actually 3 dB higher at the time of the SHG measurement (which is

in the range of possible output powers at 1955 nm), the overall efficiency would be about 0.06/W, a much more realistic value.

3.5 PPLN Conclusions

The purpose of the PPLN experiments was to measure the center wavelengths and efficiencies of non-linear devices in order to find devices that are optimal for f-2f self-referencing. Many devices on multiple chips were assessed using different inputs to initially classify the devices. From the collected data, Chip 6 Device 13 was a viable option to complete the self-referencing due to its conversion wavelength of ∼978 nm, its output power of -30 dBm, and its overall efficiency of 0.056/W. In order to complete classification of the SRICO devices more will need to be tested using the commercial laser.

4. RADIO FREQUENCY INSTRUMENTATION AND EXPERIMENTS

4.1   Motivation

We acquired a new Keysight digital signal analyzer (DSA) as part of a grant from the US Air Force, the Keysight DSA 93004L. One goal of the following radio frequency experiments was to evaluate some of the key performance parameters of the new DSA and show how the DSA can be an asset to the optical frequency comb experiments in our lab. The DSA features 32 GHz of bandwidth and a real time fast Fourier transform function. Details about the performance of the DSA can be found starting in section 4.3.

When evaluating the locks that stabilize an optical frequency comb, the signal to noise ratio (SNR) is an important parameter. As described in the introduction, optical frequency combs provide an interface between optical frequencies and radio frequencies. Therefore, a significant portion of the clock analysis occurs in the radio frequency (RF) domain. Each measurement instrument introduces a varying amount of noise known as the instrument noise floor, and in order to be confident in the SNR of a measurement, the instrument noise floor must be known and compensated for in an experiment.

In addition, the signals involved in RF locks occur at various spans with varying separations and linewidths; therefore, an instrument must possesses enough resolution to resolve a signal for analysis. If a signal drifts greatly or there is a large frequency separation between signals, a larger span must be employed on the instrument in order to capture two relevant parts of a signal. This increase in span reduces the resolution of the measurement – when using an instrument that provides a fixed number of output data points.

For the work described in this chapter the instrument noise floor of both a digital signal analyzer and an electronic spectrum analyzer (ESA) were evaluated. The second part of the RF experiment determines which instrument (the DSA or the ESA) would be better for observing large bandwidth signals. This chapter will focus on how spectrum analysis tools

function and how their capabilities can be leveraged towards evaluating the optical frequency combs required for optical atomic clocks.

4.2 Radio Frequency Instrument Theory

4.2.1 Thermal Noise, Signal to Noise Ratio, Noise Figure, and Resolution Bandwidth

Due to the random motion of electrons, noise is introduced to a system naturally. Thermal noise is based on bandwidth; therefore, it is often represented as a power spectral density on a per Hz basis. The thermal noise spectral density is described by the following equation where k_B is Boltzmann's constant and T_s is the standard noise temperature of 290 kelvin [24]:

$$P_{noise} = 10\log(k_B T_s) \tag{4.1}$$

Noise is temperature dependent; therefore, as temperature increases, so too does the noise. Evaluating equation 4.1 (assuming room temperature) results in a noise power spectral density of -174 dBm/Hz. The thermal noise floor can be calculated by using this thermal noise spectral density and multiplying it by a particular bandwidth.

The signal to noise ratio (SNR) is a measurement of the signal power compared to the noise power of a system. It is represented by equation 4.2. The SNR is limited by the power of the signal and the power of the noise. A better SNR is achieved when the power of the signal is increased or the noise is reduced. The noise can be reduced by reducing the temperature of the system or using low noise components.

$$SNR = \frac{P_{signal}}{P_{noise,system}} \tag{4.2}$$

An SNR value greater than one is favorable because it indicates that the signal power can be distinguished from the noise. SNR is an important metric for optical frequency comb work because higher SNR clock outputs will contain less noise. In addition, the feedback

loops used to stabilize the optical frequency combs require a particular SNR value in order to operate. As a result, it is important to understand where the noise is originating in order to account for it.

The noise figure of an instrument is one way to quantify the noise performance of the instrument at a particular center frequency. The noise figure characterizes the degradation of the SNR of an instrument or device [25] and is the difference between the thermal noise floor and the instrument noise floor. In general, a small noise figure is advantageous because then the instrument or device is not introducing as much noise to the system. Equation 4.3 shows how to calculate the noise figure. In the expression, "G" represents the gain of the device and N_{out} is the output noise value. "nf" is the noise factor of the system and NF is the noise figure.[24]

$$nf = \frac{N_{out}}{GN_{Thermal}}, NF = 10\log(nf) \tag{4.3}$$

For a system containing multiple cascaded devices, the noise factor equation is determined by equation 4.4 [25].

$$nf_{total} = nf_1 + \frac{nf_2 - 1}{G_1} + \frac{nf_3 - 1}{G_1 G_2}.... \tag{4.4}$$

where the values of nf are the numerical noise factor of the component and G is the numerical gain of a component. When the noise factor of an instrument is minimized, the SNR of the measurement is improved. This is because a smaller noise factor means that less noise is introduced by the instrument.

Another important parameter in measuring RF signals is the resolution bandwidth (RBW) of the measuring instrument. In the frequency domain, this metric determines how much frequency spacing is required between two signals in order for them to be resolved as two separate signals by an analyzer[26]. The smaller the resolution bandwidth value, the closer together in frequency two signals can be and still be resolved. In an instrument, the reso-

lution bandwidth determines the width of the intermediate frequency (IF) filter applied to the signal (see section 4.2.3). The resolution bandwidth is analogous to radar resolution in that the resolution of a radar determines how far apart two objects (e.g. fighter aircraft) must be in order for the radar to determine they are two separate objects. As the resolution bandwidth decreases, the displayed thermal noise floor is reduced. Table 4.1 shows the value of the thermal noise floor at various resolution bandwidths. As a result, a smaller RBW improves the noise floor of a system.

Table 4.1. Resolution bandwidths and corresponding thermal noise floors

RBW	Thermal Noise Floor
1 Hz	-174 dBm
100 Hz	-154 dBm
1 kHz	-144 dBm
100 kHz	-124 dBm
1 MHz	-114 dBm

4.2.2   The Fast Fourier Transform, Filtering, and Windowing

When a Fourier transform is taken using electronics (like the instruments described in the next section), the fast Fourier transform (FFT) algorithm is employed. The FFT is an algorithm that utilizes the discrete Fourier transform (DFT) to transform sampled data points from the time domain to the frequency domain. This tool is advantageous for computers and hardware applications because it works for finite length discrete signals. The DFT can be expressed as [27]:

$$\tilde{X}[k] = 1/N \sum_{n=0}^{N-1} x[n] \mathrm{e}^{-2\mathrm{j}k(2\pi/N)n} \tag{4.5}$$

The FFT is employed by oscilloscopes and other spectrum analysis tools in order to transform time domain data into the frequency domain. The FFT is an important function for the experiments described in this chapter since we will need to convert the time domain trace of an oscilloscope to the frequency domain trace of an analog spectrum analyzer.

In order to analyze signals, it may be required that a particular frequency or time domain component is isolated. This is achieved by filtering in the frequency domain and windowing in the time domain. Filtering involves convolving a time domain signal with a transfer function (which serves as a filter). Based on the Fourier property [28]:

$$x_1(t) * x_2(t) \Leftrightarrow X_1(f)X_2(f) \tag{4.6}$$

the convolution in the time domain is a multiplication operation in the frequency domain. The definition of the continuous Fourier transform and the continuous inverse Fourier transform is as follows [27]:

$$x(t) = 1/2\pi \int_{-\infty}^{+\infty} X(j\omega)e^{j\omega t}d\omega \tag{4.7}$$

$$X(j\omega) = \int_{-\infty}^{+\infty} x(t)e^{-j\omega t}dt \tag{4.8}$$

Windowing is a similar operation to filtering; however, the difference lies in which domain the convolution occurs. When using a window, the signal and transfer function (window) are convolved in the frequency domain and multiplied in the time domain [29]. Therefore, the relationship between the time and frequency domain is:

$$x_1(t)x_2(t) \Leftrightarrow X_1(f) * X_2(f) \tag{4.9}$$

The next section will describe the basics of spectrum analyzer tools that utilize the definitions from this section and introduce the basics of RF instruments employed to carry out this work.

4.2.3 Instrument Device Fundamentals

In our lab, in order to evaluate the a noise floor, signal to noise ratio or frequency composition of a signal, two devices are available to use in the analysis. The first device is an oscilloscope and the second device is a electronic spectrum analyzer (ESA). A digital oscil-

loscope samples an analog signal using an analog to digital converter (ADC) and discretizes the waveform. The number of bits in this analog to digital converter determines the vertical resolution of the oscilloscope. An analog to digital converter with more bits possesses more quantization levels; therefore, it will have finer vertical resolution and a lower amount of introduced noise. This relationship is described by equation 4.10 where σ^2 is the noise power and "B" is the number of bits [29]. While increasing the number of bits reduces the noise power, it will increase the data processing time, display time, and transfer time.

$$\sigma^2 = \frac{2^{-2B}}{3} \tag{4.10}$$

This sampled signal is the time domain representation of the signal. In order to obtain frequency-domain representation, an oscilloscope can mathematically calculate the FFT of the time domain signal. The FFT is a signal processing algorithm that utilizes the DFT as referenced in section 4.2.2.
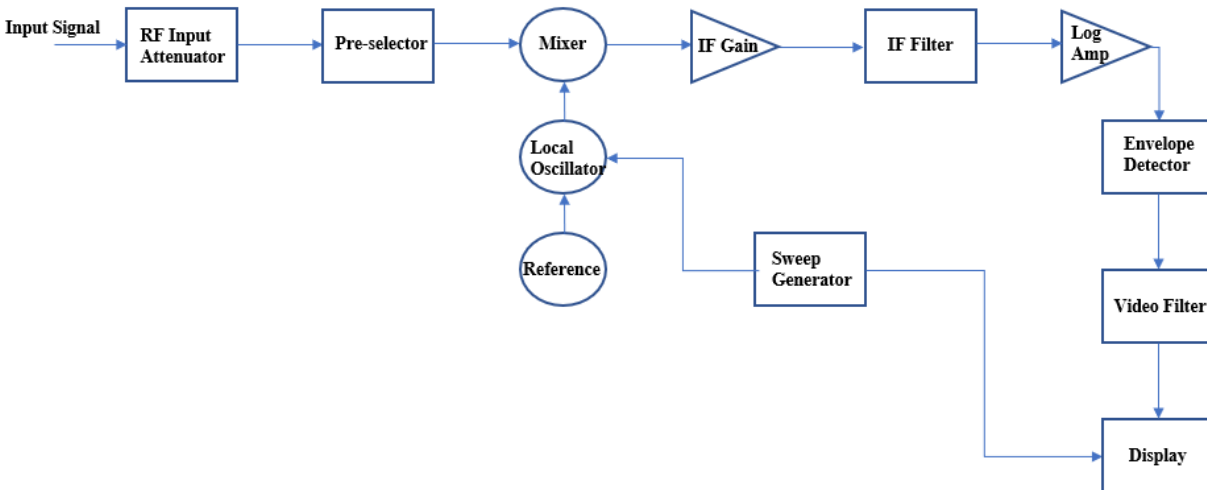
Figure 4.1. Schematic of a basic spectrum analyzer. Based off of schematic found in [26].

An electronic spectrum analyzer differs from an oscilloscope in that it functions like a superheterodyne receiver where a local oscillator is swept and mixed with the incoming signal. This signal is then processed and filtered in order to derive the frequency information. Unlike

an oscilloscope, it does not mathematically compute the FFT of a time domain signal, it measures the spectrum directly. Figure 4.1 shows a basic schematic for a spectrum analyzer. First the signal passes through an attenuator so that powerful signals do not damage the internal electronics of the device. Many spectrum analyzers contain a pre-selector which limits the input signal to the desired frequency range. This prevents undesired frequencies, outside of the desired bandwidth, from mixing with the desired signals. The signal is then mixed with local oscillator (LO) signal, and alterations to the local oscillator frequency are enacted by a sweep generator. Simple signals, such as a single sinusoidal tone, can be related to the local oscillator by equation 4.11 [28].

$$A\cos(\omega_1) * B\cos(\omega_2) = \frac{1}{2}AB\cos(\omega_1 - \omega_2) + \frac{1}{2}AB\cos(\omega_1 + \omega_2) \qquad (4.11)$$

After being mixed, the signal passes to the intermediate frequency (IF) gain and intermediate frequency filter. The IF gain sets the reference level for the signal. The IF filter is a bandpass filter that rejects the LO, and the undesired mixing products from the sweep. The RBW of the spectrum analyzer measurement establishes the frequency width of this IF filter. In some cases a logarithmic amplifier is utilized to control the gain over a large signal band. Logarithmic amplifiers are able to handle larger frequency bandwidths and dynamic ranges [30]. Logarithmic amplifiers also help normalize the data for display on a logarithmic scale. The signal then goes to a envelope detector (or mathematically equivalent system) to sample the voltages. Finally, before going to the display, the signal passes through a video filter. The video filter is often a low pass filter where the bandwidth is referred to as the video bandwidth (VBW). If the VBW is much smaller than the RBW, then the signal can be smoothed. Section 4.4.2 on the ESA characterization will show an example of this video averaging.

The speed at which a spectrum analyzer can sweep across a span is determined by the span length and the resolution bandwidth. For an analog spectrum analyzer, the sweep time can be determined by the following equation: [26]

$$\text{sweep time} = \frac{k * span}{(RBW)^2} \tag{4.12}$$

where k is a proportionality constant for the device. Many modern spectrum analyzers use faster digital filters in order to reduce this sweep time. Since the sweep time is dependent on the RBW, there exists a trade off between the resolution of a measurement and the time it takes to acquire the data. While smaller RBWs can resolve more closely spaced signals, the amount of time to acquire the data will be increased by the square of the RBW improvement. As a result, there are cases when it will not be advantageous to use an instrument's maximum RBW because the time of acquisition will outweigh the benefits of the increased resolution. For example, if two signals are separated by 1 MHz, a 1 Hz RBW would not be required to resolve the signals. It would result in long acquisition time compared to a more reasonable 100 kHz RBW.

4.2.4   Data Smoothing

This section focuses on how the DSA and ESA noise floor data was processed. Further details on the DSA and ESA's respective noise floors is found in section 4.4. In both of these devices, the noise varies between 20 dBm and 30 dBm which makes it hard to pinpoint the exact value of the noise floor. Therefore, data smoothing was employed to reduce the variation in the noise. There are a number of different strategies that can be employed to accomplish this goal, but two were utilized for this experiment.

The first algorithm is an average. On the ESA, smoothing was implemented by employing a video average. As previously described, video averaging employs a video filter and takes advantage of the ratio VBW « RBW. The DSA has a similar averaging function where the number of averages can be set by the user. The more averages that are included in the

measurement, the smaller the variation in the noise floor. However, on both devices, increasing the number of averages also increases the computation time to take a measurement. An example on the ESA is shown in figure 4.2(b).

The other algorithm that was employed on the DSA is a window function on the noise floor (see section 4.2.2). The FFT noise floor was recorded by a MATLAB interface and then a python program performed the window function. The FFT data was reverted to a time domain signal by using the IFFT. Then the data points were multiplied by a Gaussian window in the time domain. After the window was applied, the data was transformed back to the spectral domain. Equation 4.13 highlights the equation for a Gaussian window where τ is the width of the window.

$$w(n) = \mathrm{e}^{\frac{-t^2}{\tau^2}} \tag{4.13}$$

As the width of the window is reduced, the amount of smoothing increases as the window approaches a delta function. Figure 4.2 (a) shows the difference in smoothing on the DSA instrument noise floor data using different window sizes. In this example, the record length was 249,034 and the frequency bin spacing was ∼76 kHz.

4.3 DSA 93004L Interface and Characterization

As mentioned in the motivation, one of the instruments evaluated in the RF noise work is the Keysight digital spectrum analyzer 93004L (DSA). This instrument possesses 32 GHz of RF bandwidth and a real time FFT feature that can be utilized to evaluate spectral components of a signal. In order to record the data from the DSA an interface with MATLAB was achieved. The interface is facilitated by a virtual instrument software architecture (VISA) connection. The MATLAB scripts were adapted from Dr. Dan Leaird's Keysight oscilloscope code and adjusted to handle the nuance of the DSA 93004L. The DSA transmits the information using a preamble where each entry in the structure contains a characteristic of the data (e.g. x and y axis intervals). When handling the data directly, many of the data points associated with the highest peak powers are inverted (i.e. the data points with the
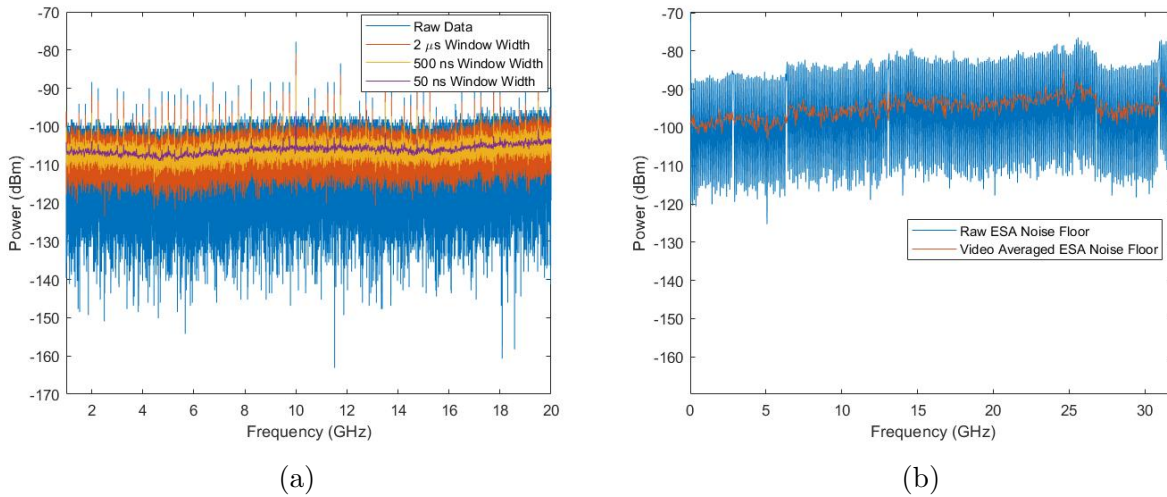
Figure 4.2. (a) Windowed DSA noise data showing the impact of window size on smoothing. The resolution bandwidth of the noise floor measurement is 150 kHz. (b) Impact of 9 video averages on the ESA noise floor trace (RBW: 100 kHz).

highest magnitude, appear as the lowest). Therefore, the MATLAB code mathematically adjusts these points in order for the recorded data to match the DSA screen.

The DSA has the ability to record data that exists both on the channels and the functions (such as the FFT). When either the time domain channel or a function is pulled via MAT-LAB, the DSA sends data for the entire sampling rate divided by 2 even if it exceeds the range displayed on the screen itself or the bandwidth itself. For example, pulling the FFT data using MATLAB at 80 Gsamp/s will plot 40 GHz of information even though the DSA bandwidth is 32 GHz. If the user wants to focus on a specific span of time or frequency, the DSA contains a gating function that is used to reduce the data samples collected by MATLAB. A gating function bounds the collected data points that are transferred using the MATLAB interface. On the DSA this function can be applied to either the time domain data or the frequency domain data to reduce the number of points represented in MATLAB.

Figure 4.3 shows a 5 GHz sinusoid (provided by a frequency synthesizer –see section 4.5.1 for more information on the frequency synthesizer) recorded using the FFT function on the

DSA. Figure 4.3 (a) shows the result of taking the FFT data directly using MATLAB. Figure 4.3 (b) illustrates the same tone, but utilizing the gating function on the DSA to limit the data set.

(a)   (b)
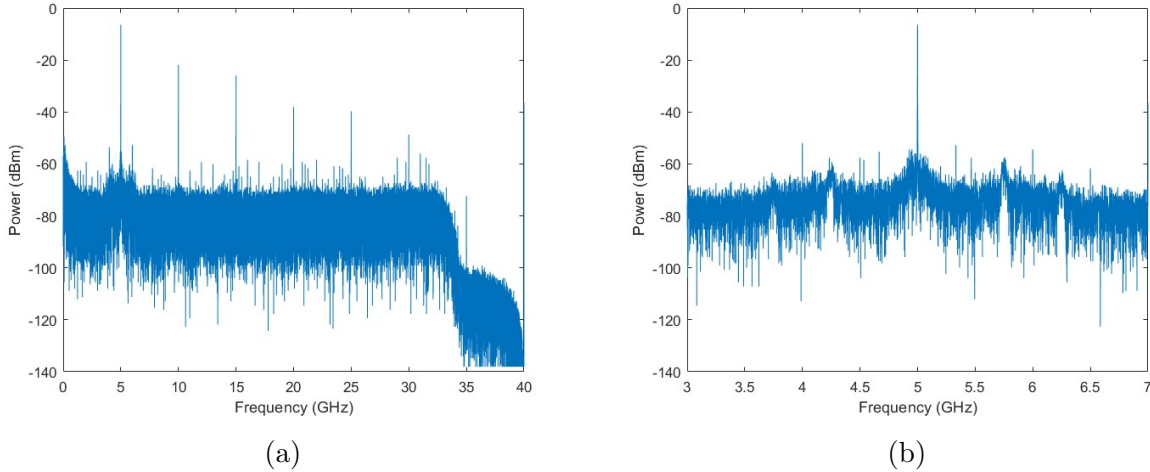
Figure 4.3. DSA FFT MATLAB plot of a 5 GHz signal with a RBW of 750 kHz. (a) shows the MATLAB FFT plot without any gating implemented. The function is not gated so the entire spectrum is recorded independent of the DSA screen configuration. (b) shows the same spectrum with a fixed gate applied to reduce the display range from 0-40 GHz to 3-7 GHz.

Similar behavior occurs with recording the data of the time domain signal, and other mathematical or filtering functions. Therefore, if a user wants to record the same information as it appears on the screen, they must set a gating function to match the bounds on the screen.

When operating two channels, the DSA has a maximum sampling rate of 80 GSa/s and when operating all four channels the maximum sampling rate is 40 Gsa/s. At 80 Gsa/s, the instrument records 40 GHz of data even though 40 GHz exceeds the maximum 32 GHz of bandwidth possible. Reducing the sampling rate and therefore the allowable bandwidth reduces the frequency range of the resultant MATLAB plot. For example, if the sampling rate is manually set to 40 Gsa/s than the resultant MATLAB plot without gating will be from 0 Hz - 20 GHz. Even though the Nyquist rate could theoretically allow the maximum

frequency to be 20 GHz, the DSA has a 0.8-0.84 factor built in to the bandwidth. Therefore, 80 Gsa/s provides 32 GHz of bandwidth and 40 Gsa/s provides 16.8 GHz of bandwidth. This is to ensure that the signals can appear smooth on the screen and account for any anti-aliasing filters that may exist within the DSA.

4.4   Instrument Noise Figure

Different instruments exhibit different noise characteristics due to their detectors, internal electronics, and digital signal processing algorithms. As a result, understanding the intrinsic noise characteristics of an instrument is vital to accurately compute the SNR of a signal. In order to fully stabilize a frequency comb, as explained previously, an understanding of the SNR of the locking signals is required. Therefore, knowledge of the noise floor and noise figure of the measuring instrument are vital.

4.4.1   DSA

The noise floor of the DSA was measured by terminating the input to channel 1 with a 50 Ω load and using the built in FFT function to generate the frequency spectrum. As described in the next section, the ESA specifies the noise floor in the spectral domain in units of dBm. Therefore, in order to compare the noise performance of the two devices, the noise floor of the DSA was evaluated in the spectral domain after the FFT was taken of the time domain data. Keysight specifies the noise floor of the instrument in the root mean squared voltage (V_{RMS}) at a particular vertical resolution setting and the following discussion describes how to convert from V_{RMS} to an FFT noise floor.

First the RMS voltage is converted to power by:

$$P_{noise} = \frac{V_{RMS}^2}{R} \tag{4.14}$$

where the resistance is the 50Ω load in the DSA. The power is then converted to a noise spectral density in units of W/Hz by dividing the total bandwidth of the DSA settings. The specification provides the power spectral density (PSD) at particular bandwidths (BW).

$$PSD = \frac{P_{noise}}{BW} \tag{4.15}$$

The noise floor is determined on a per Hz basis; therefore, in order to determine the noise floor power, the PSD is multiplied by the RBW of the measurement.

$$P_{noise floor,W} = PSD * RBW \tag{4.16}$$

Finally, the noise floor power can be converted to dBm by:

$$P_{noise floor,dBm} = 10 log(\frac{P_{noise floor,W}}{1mW}) \tag{4.17}$$

The V_{RMS} values specified in the datasheet were converted to dBm noise levels (using equations 4.14-4.17 above). The values were then compared to the FFT noise floor values on the DSA. Since the FFT noise floor varies by up to 40 dB [see Raw Data trace in figure 4.2 (a)], the built in smoothing function (using an average) was employed to reduce the variation in the noise. However, even at a particular bandwidth, the noise floor is not completely flat; therefore, the measured noise floor values are best estimates using the marker tools on the DSA. A sample of the comparison is shown in Table 4.2 using two different vertical resolutions, two different bandwidths, and two different RBWs.

The specified noise floor (converted to dBm) reasonably agrees with the measured data on the DSA FFT function. Any disparities between the values are likely attributed to the noise floor varying slightly with respect to frequency, and that these values are estimated using a marker at the top of the smoothed FFT function.

The noise figure of the instrument can be determined by comparing the instrument noise floor with the thermal noise floor at a particular bandwidth. Since the instrument noise

Table 4.2. Specified and measured noise floor values for the DSA 93004L

Vertical Resolution (mV/div)	Resolution Bandwidth	Bandwidth (GHz)	Specified Noise Floor (dBm)	Observed Noise Floor (dBm)
20	150 kHz	16	-97.27	-97.203
20	150 kHz	30	-97.007	-97.1
200	150 kHz	16	-77.65	-77.02
200	150 kHz	30	-77.52	-77.2
20	1.5 MHz	16	-87.27	-88.02
20	1.5 MHz	30	-87.0774	-86.53
200	1.5 MHz	16	-67.6246	-67.87
200	1.5 MHz	30	-67.523	-66.53

figure characterizes the noise introduced to the system by the instrument, the difference between the instrument noise floor and the thermal noise floor is the instrument's noise figure. At 150 kHz RBW, the thermal noise floor is -122.23 dBm. Therefore, the noise figure with a vertical resolution of 20 mV/div is ∼25 dB and with 200 mv/div is ∼45 dB. At 1.5 MHz RBW the thermal noise floor is -112.2 dBm; therefore, the corresponding noise figures are once again about 25 and 45 for 20 mV/div and 200 mV/div respectively.

As shown by table 4.2, the noise figure will adjust as a result of the vertical resolution setting changing. This is because the finite number of bits in the ADC must represent a wider voltage range when the voltage per division is increased. As a result, more noise is introduced to the system as the vertical quantization bins become larger. Therefore, to reduce this quantization noise, when taking a measurement, use the smallest possible vertical division setting that does not clip the signal. However, table 4.2 also shows that the noise figure does not change as a function of resolution bandwidth. This is expected because the RBW will scale the thermal noise floor and the instrument noise floor in conjunction; therefore, the noise figure will remain the same. For a particular vertical division setting, the noise figure between 150 kHz and 1.5 MHz is consistent. The resolution bandwidths of 150 kHz and 1.5 MHz were chosen because when the DSA automatically adjusts the sampling rate and memory depth for the real time FFT these are two of the possible RBW settings.

Figure 4.4 displays the noise floor at resolution bandwidths of 100 kHz and 1 MHz. The noise floor variation was reduced by implementing the windowing technique described in Section 4.2.4. The window size employed was 100 ns. These resolution bandwidths were selected in order to compare the noise floor results to the the ESA as shown in figure 4.7. On the DSA, the sampling rate and memory depth need to be set to manual in order to select these RBWs.
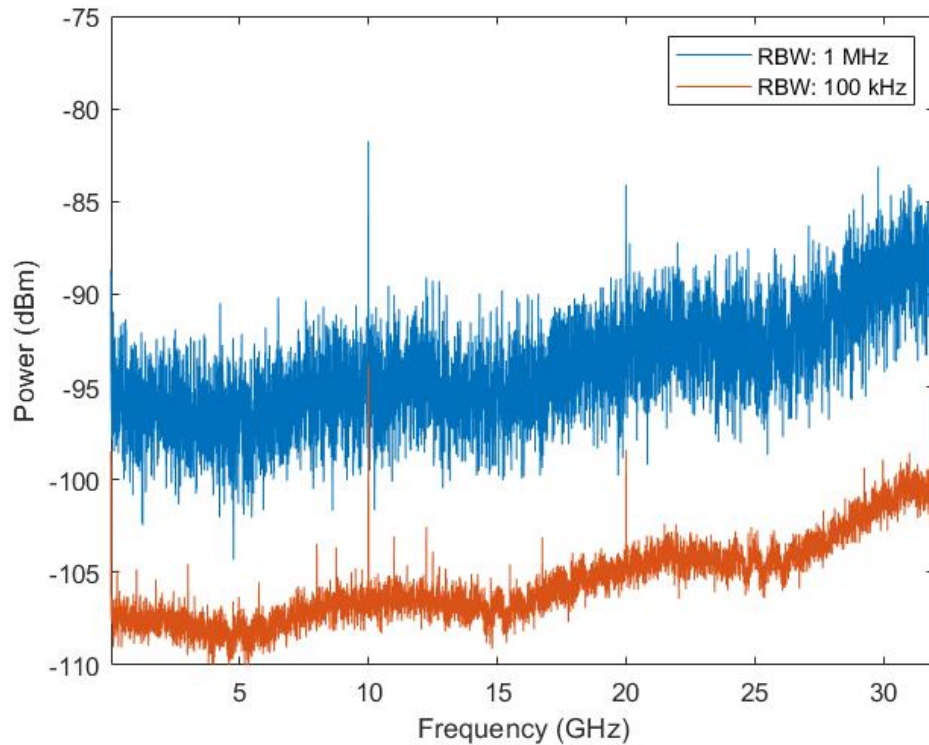
Figure 4.4. DSA noise Floor at resolution bandwidths 100 kHz and 1 MHz.

Figure 4.4 shows that the noise floor of the DSA is resolution bandwidth dependent. This is consistent with equation 4.16. As a result, the noise floor is reduced if a lower resolution bandwidth is employed. However, in order to implement these finer resolution bandwidths, the DSA requires a greater amount of memory points and a longer sweep time. Therefore, there is a trade off between the instrument noise floor level and the time that it will take for the FFT to be performed. When taking a measurement, one should consider the expected resolution of the signals and adjust the resolution bandwidth to be a smaller value. However,

if the resolution of the signals is 1 MHz, then there may not be a requirement for a very small and time consuming resolution bandwidth such as 1 kHz.

The vertical resolution setting on the DSA is an important consideration when capturing the data with MATLAB. When only noise is present, the DSA must be configured to 1 mV/-div of vertical resolution in the time domain (the minimum setting). Larger vertical settings cause the resultant FFT data, sent to MATLAB, to be higher than the value displayed on the actual screen of the DSA. Altering the vertical resolution adds between 5 and 10 dB of difference for each increment until the difference is 25 dBm. This difference between the display and the MATLAB plot has a maximum value of 25dB at the maximum resolution setting of 1 V/div. This phenomenon does not occur when a -50 dBm or greater signal is present at the input of the channel; therefore, for nominal use the vertical resolution should be adjusted to prevent clipping if a signal of -50 dBm is present.

In order for input noise to exceed the instrument noise, an amplifier with sufficient gain is required to surpass the instrument noise figure. This is important because if the signal (which is the thermal noise level for this experiment) is above the instrument noise level, then the input noise will dominate. This means that the input noise can be characterized without being lost in the instrument noise floor. The amplifier chosen was the Mini-circuits ZVE-3W-183+ High Power Amplifier. This amplifier has a specified gain range of 29 dB to 40 dB, a specified operational range of 5.9 GHz to 18 GHz, and a specified noise figure of 5.5 dB. For the purposes of this experiment, the specified noise figure of the amplifier was utilized; however, the experimental noise figure of the amplifier could be measured by using a calibrated noise source as the input to the amplifier and determining how the noise is altered by the amplifier. The Y factor technique is one method that could be chosen to complete this experimentally. The Y factor technique compares the noise power when the noise source is turned on and turned off. It allows for a noise temperature to be calculated, which in turn, determines the noise figure [28].

The gain profile of the amplifier was measured using a vector network analyzer (VNA). A VNA generates a known test signal and utilizes a receiver to measure the throughput and reflection of a test device. For this measurement, the VNA passes a signal through the amplifier and determines the frequency response of the amplifier. When measuring a gain profile, the input signal power must be small enough to prevent saturation of the amplifier. If the amplifier is saturated, it will not provide the maximum allowable gain. Figure 4.5 shows the resultant gain profile.
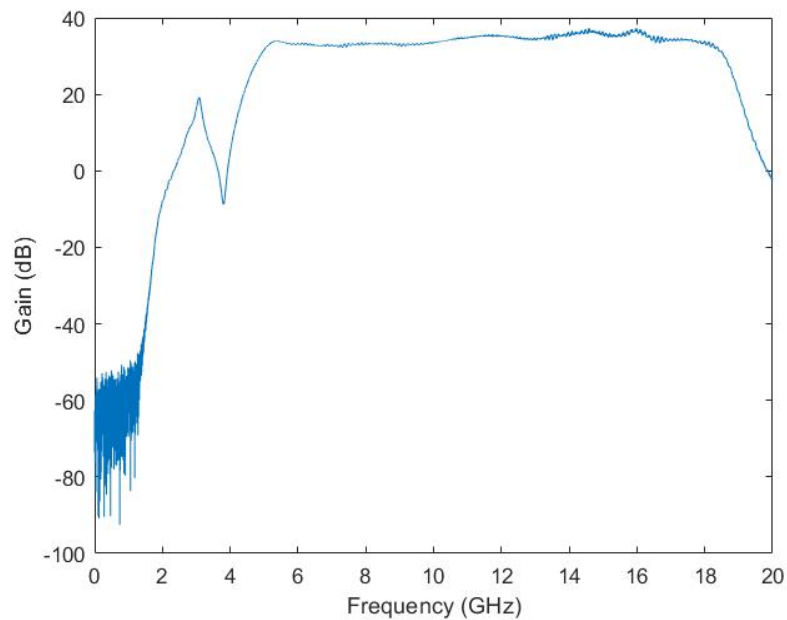
Figure 4.5. Gain Profile of ZVE-3W-183+ Amplifier

The measured gain profile confirms the operational range of the amplifier and also confirms that the actual device operation is within the range specified by the manufacturer (29 dB - 40 dB in the operational range of 5.9 GHz - 18 GHz).

To measure the amplified thermal noise floor, the input of the amplifier was terminated with a 50 Ω load and the output of the amplifier served as the input to the DSA. Figure 4.6 displays the resultant amplified noise floor compared to the instrument noise floor at 100 kHz RBW. This figure also shows the expected thermal noise floor level based on the RBW,

the thermal noise level, the measured gain profile of the amplifier, and the specified noise figure of 5.5 for the amplifier. This relationship is characterized by equation 4.18.

$$\text{Theoretical Amplified Noise Level} = -174dB + 10\log(RBW) + G_{amp} + NF_{amp} \quad (4.18)$$
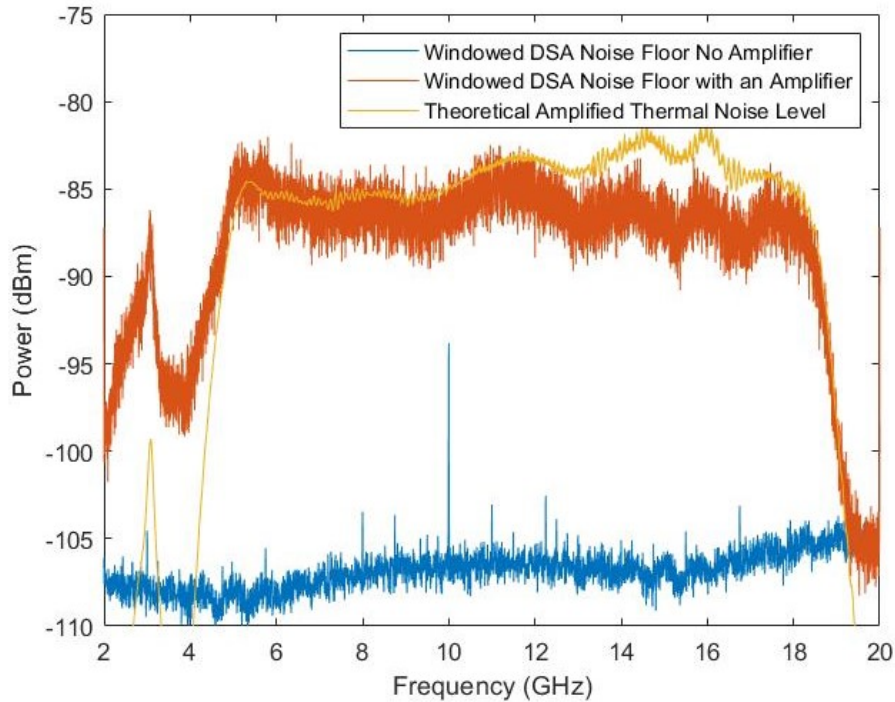
Figure 4.6. Comparison of the DSA instrument noise floor with the amplified thermal noise floor and the expected amplified thermal noise floor (calculated using equation 4.18). The DSA traces were windowed using the algorithm described in Section 4.2.4. The resolution bandwidth is 100 kHz.

In figure 4.6, when the theoretical amplified noise level was calculated, it assumed that the noise figure of the amplifier was consistently 5.5 dB for the entire operational bandwidth. In reality, the noise figure of the amplifier likely has some variation throughout the operational frequency range. In addition, amplifiers can saturate if the input power is too large, which reduces the gain. Since the input to the amplifier is a broadband noise signal, the amplifier may saturate at higher frequencies. As a result, the measured input noise level may be lower than the gain measured using the VNA when a broadband signal is introduced to the amplifier.

4.4.2 ESA

The electronic spectrum analyzer (ESA) utilized in these experiments is the Agilent 8565EC electronic spectrum analyzer. The ESA noise floor is specified, by the manufacturer, in terms of the displayed average noise level (DANL). The displayed average noise level is the average noise value over a specific frequency range when the input is terminated with a 50 Ω load and referenced to 1 Hz. This is analogous to an instrument noise floor with a RBW of 1 Hz. This value is used to describe the noise floor of a spectrum analyzer. The DANL value is dependent on center frequency and will change through the entire operational bandwidth of the spectrum analyzer. The specified noise figure can be derived by comparing the difference between the thermal noise level at 1 Hz RBW (-174 dBm) and the DANL value for a specific center frequency. Table 4.3 shows an example of the DANL specification and the corresponding noise figure.

Table 4.3. Displayed average noise level and noise figure specifications for the Agilent 8565EC

Frequency	Specified DANL (dBm)	Noise Figure (dB)
6 GHz	-147	27
13 GHz	-143	31
17 GHz	-140	34
20 GHz	-140	34

In order to experimentally verify the ESA noise floor, the input was terminated using a 50 Ω termination. The noise floor was then measured using a 20 GHz span at a few RBW values. At 100 kHz of RBW the noise floor possess approximately 25 dB of variation. The ESA includes a video averaging function that reduces this variation using an average as described in section 4.2.4. Table 4.4 shows the noise floor and noise figure at 100 kHz and 1 MHz of RBW. The data is an average of two sets of ESA noise data taken on two separate occasions. One set of data only had one video average applied to it. The other had nine video averages applied to it in order to reduce data variation. The measured noise floor at 100 kHz RBW and 1 MHz RBW and the associated noise figure is summarized in table 4.4.

Table 4.4. Measured noise floor and noise figure at 100 kHz RBW and 1 MHz RBW for the Agilent 8565EC ESA

Frequency (GHz)	RBW	Measured Noise Floor (dBm)	Measured Noise Figure (dB)
6	100 kHz	-96.75	27.25
13	100 kHz	-94.08	29.92
17	100 kHz	-91.5	32.5
20	100 kHz	-93.16	30.84
6	1 MHz	-86.93	27.07
13	1 MHz	-83.99	30
17	1 MHz	-81.99	32
20	1 MHz	-82.08	31.92

The measured results shows that the noise figure increases with the center frequency, but remains independent of the RBW. This result is consistent with the specified characteristics from the manufacture and is a comparable result to the DSA. Figure 4.7 shows an exampled of the noise floor at two sample RBWs. In the figure the noise floor was smoothed using 9 video averages, then the data was exported to MATLAB. The span was set to 32 GHz in order to match the total bandwidth of the DSA in figure 4.4.

Similar to the DSA experiments the ZVE-3W-183+ amplifier was employed to elevate the input noise level above the instrument noise level. Figure 4.8 illustrates the difference between the instrument noise floor and the thermal noise floor after utilizing the amplifier. As described before, the expected thermal noise floor utilizes the thermal noise value of -174 dB/Hz, adds the gain of the amplifier, adds the noise figure of the amplifier, and adds the thermal noise adjustment based on the RBW (see equation 4.18).

Similar to figure 4.6, the discrepancy between the theoretical amplified thermal noise floor level and the ESA trace in figure 4.8 could be attributed to the noise figure of the amplifier deviating from the specified value at higher frequencies. Since, the theoretical level is higher than the amplified thermal noise measured with both the DSA and the ESA, the amplifier noise figure is likely lower than the specification as the frequency increases. Also similar to the DSA, it is possible that the amplifier is being saturated by the broadband
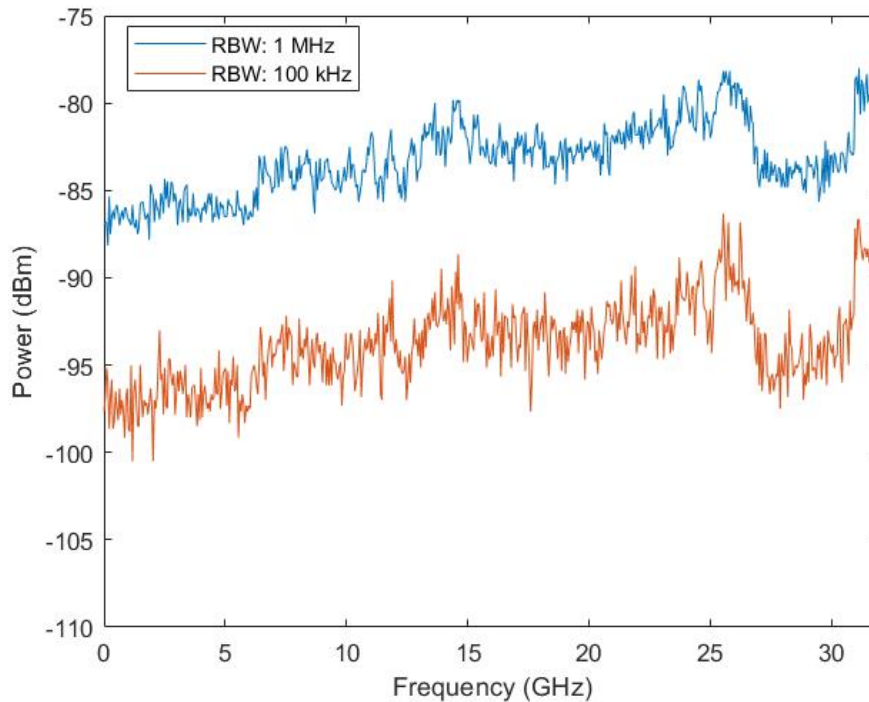
Figure 4.7. Measured ESA noise floor at 100kHz and 1 MHz of RBW. The raw noise floor data was processed using the video-averaging function on the ESA.

thermal noise input. However, with only about 13 GHz of bandwidth on the amplifier, the gain is likely not large enough to amplify the thermal noise level to the point of saturation.

Overall, the DSA has a noise figure that is ∼10 dB lower than the ESA and possesses a noise floor that is ∼10 dB lower than the ESA at ∼100 kHz RBW. This means that the noise performance of the DSA is better than the ESA under the circumstances tested here.

4.5 Frequency Resolution Measurements

The DSA and ESA each possesses different frequency bin spacing algorithms which affects the resolution of the captured measurements. The goal of the following frequency resolution measurements was to quantify this difference in frequency bin spacing and apply it to optical frequency comb experiments. The frequency resolution of the DSA FFT function is
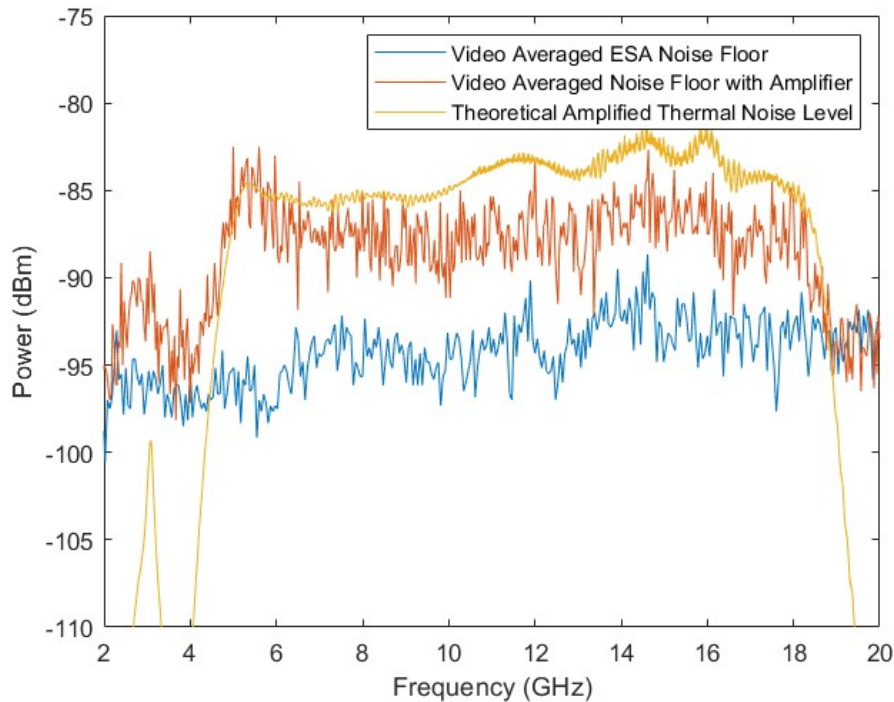
Figure 4.8. Comparison of the ESA noise floor with the amplified thermal noise floor and the theoretical amplified noise floor. The RBW of the ESA is 100 kHz.

dependent on both the sampling rate and the number of samples recorded across the entire bandwidth. The resolution is the sampling rate divided by the number of points collected. The individual spacing between each point is one half of the frequency resolution. The DSA possesses the ability to manually set both the sampling rate and the memory depth of the data capture. Due to the Nyquist limit, the DSA must sample at least 64 GSa/s in order to capture the entire 32 GHz of bandwidth. However, the DSA possesses a higher real-time sampling rate of 80 GSa/s when using one or two channels. The DSA also records up to 100 Mpts on 2 channels. The user has the ability to set either parameter.

Since the memory depth can be adjusted, the number of points that the DSA takes is based on the time span captured on the channel. The frequency spacing on the FFT function is based on the resolution bandwidth of the measurement because the resolution bandwidth of the measurement determines the length of the time sample that must be taken. Smaller

64

resolution bandwidths require longer traces to be taken. The frequency bins of an FFT are dependent on both the length of the trace (i.e. the total number of points taken) and the time interval between each point. A larger trace length will result in smaller FFT bins.

The ESA records 600 points of data independent of the RBW; therefore, the frequency spacing between each point depends on the entire frequency span captured by the ESA. For example, a frequency span of 10 MHz results in 16.6 kHz of frequency spacing. Furthermore, as explained by equation 4.12 the sweep time of the ESA is impacted by the RBW of the device. Even though the ESA employs digital filtering to measure signals, reducing the resolution bandwidth still increases the time by the square of the difference (e.g a 32 GHz trace at 300 kHz of RBW takes 890 ms compared to the same trace at 100 kHz where it takes 8s, a factor of 9 difference in sweep time).

4.5.1   Frequency Spacing Using an RF Frequency Synthesizer

In order to showcase the differences in the DSA and ESA resolutions, an experiment using a two channel frequency synthesizer was conducted. In this experiment, the two channel frequency synthesizer would generate two tones, offset by a particular frequency and then measured at various frequency spans. The two tones were combined using an RF combiner which served as the input to both the ESA and the DSA. Figure 4.9 shows a schematic for the setup.

The two channel frequency synthesizer is the Windfreak Technologies SynthHD PRO. This two channel device has a 10 MHz- 24 GHz operational range. The device includes a graphical user interface (GUI) that can be employed to configure the synthesizer on a PC. The RF combiner employed is the ZAPDQ-4+ power splitter/combiner. This device possesses a specified operational frequency range of 2 GHz - 4.2 GHz. The device also has a specified loss of 3.4 dB. For these experiments the first channel of the synthesizer was set to 3 GHz because it is in the center of the combiner's operational range.
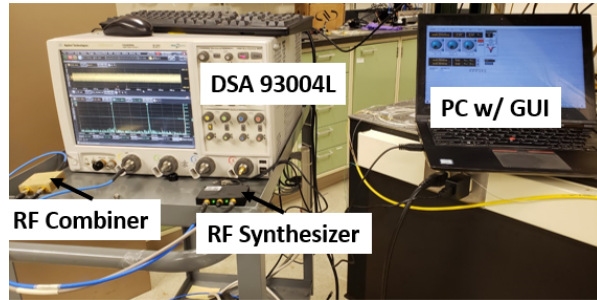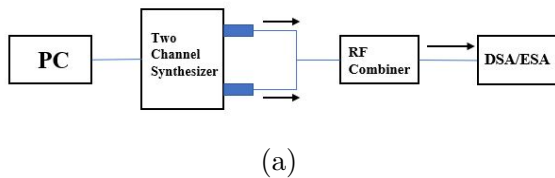
Figure 4.9. Experimental setup for instrument resolution experiments conducted with a two channel frequency synthesizer. (a) is the schematic, (b) is a photo of the laboratory setup.

With only 600 points of memory, it is expected that the best resolution that the ESA can possess is the total span divided by 600 points. When the spacing between two signals equals this ratio, the signals would be placed on two adjacent sampling points. As a result, three cases were tested for this experiment. The first is a situation when the frequency span is small enough and the distance between frequency bins is small enough that both instruments will adequately resolve both signals. The second case is close to the 600 point limitation of the ESA where the span divided by 600 will be close to the frequency separation. The third case is when the frequency separation is within the frequency bin resolution on the ESA.

Figure 4.10 shows the first case where the span is short enough and the signals are spaced far enough apart that both the ESA and DSA can resolve both peaks. In this example, the signals are separated by 50 MHz and the total measurement span is 3 GHz. The resolution bandwidth of both devices was 100 kHz. This RBW corresponds to approximately 38 kHz of frequency bin spacing for the DSA. The 3 GHz measurement span results in 5 MHz of frequency bin spacing for the ESA. With this frequency spacing, it is expected that both of the devices will be able to resolve the two signals.

Figure 4.11 shows the second case where both of the devices can resolve the two signals; however, the ESA frequency bins are not small enough to prevent a significant discrepancy between the actual separation and the measured separation of the signals. For example,

66
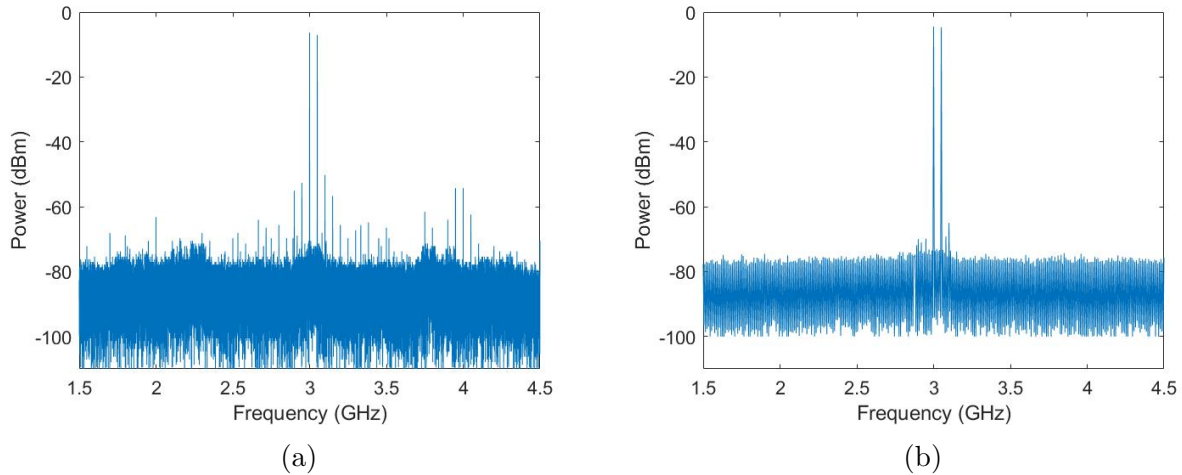
Figure 4.10. Case 1: Both the DSA and ESA resolve both signals. A signal separation of 50 MHz with the full 3 GHz span is displayed. (a) is the DSA FFT trace, (b) is the ESA trace.

with a total span of 6 GHz, the frequency spacing on the ESA is 10 MHz. Therefore, if the two input signals are spaced 10 MHz apart, then they would sit on adjacent points on the trace. Since the ESA frequency bin size is equivalent to the two times the point spacing, it will not put the signal on the adjacent point, moving it over another 10 MHz to 3.02 GHz. Since, both devices were still set to 100 kHz RBW, the DSA frequency sampling remained at approximately 38 kHz.

An important consideration for measurements from either of these devices is that the frequencies that can be measured are integer multiples of frequency bins. Therefore, if a signal does not land directly on one of these frequency bins then there will be at least some discrepancy between the measured signal and the actual signal. In order to detect every signal perfectly, there would need to be infinite frequency bins. However, in case 2 the discrepancy is much larger for the ESA than the DSA because of the frequency bin size. As either the separation between the two signals increases or the frequency bin size is reduced, the discrepancy will reduce. As an example, in Figure 4.11 the measured separation distance is twice the actual separation distance (20 MHz compared to 10 MHz). However, if the separation is increased than the discrepancy caused by the bin size is a smaller (e.g a 70 MHz separation
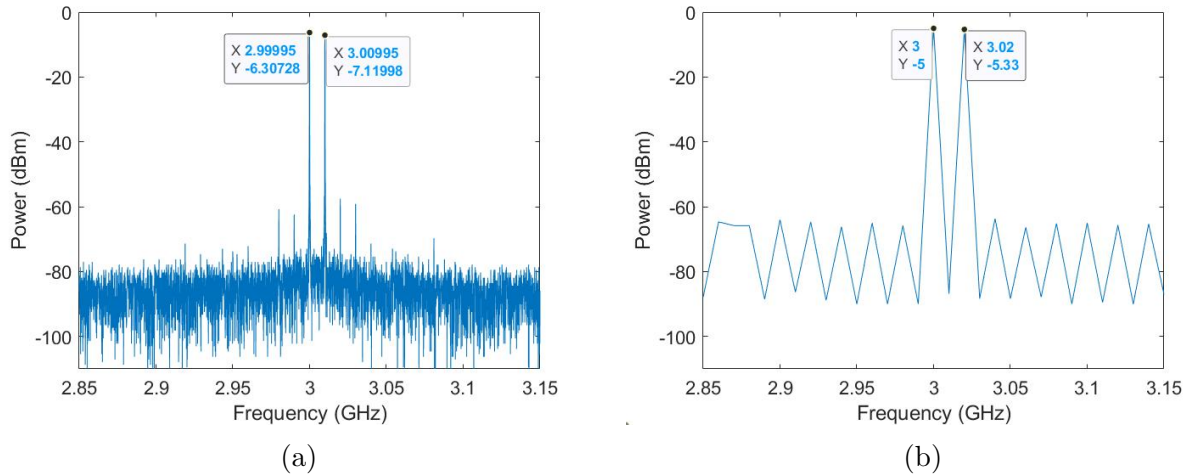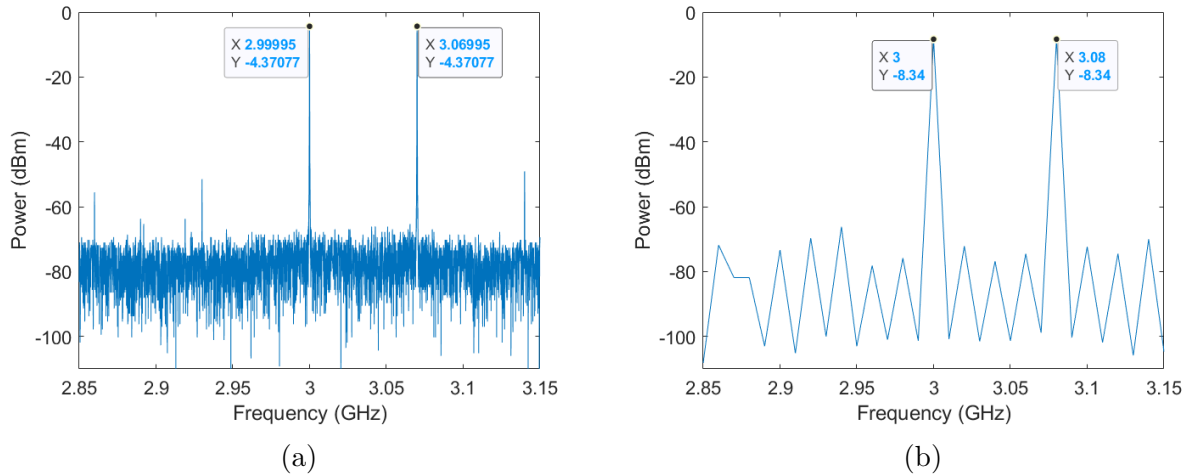
Figure 4.11. Case 2: Both the DSA and ESA resolve both signals, but the ESA aliases the separation an extra 10 MHz. The frequency axis is limited to display 300 MHz. The total span is 6 GHz and the frequency separation is 10 MHz. (a) is the DSA FFT trace and (b) is the ESA trace. The data tips are included to show the discrepancy between the actual signal separation and the measured signal separation.

will be measured as 80 MHz, see figure 4.12). Since, the DSA's frequency bins are much more fine, the discrepancy is on the order of 50 kHz as opposed to 10 MHz as seen on the ESA.

The third case shown in figure 4.13 shows the third condition where the signals are within the frequency spacing on the ESA due to the 600 point limit. In this example, the total span of 1.2 GHz results in 2 MHz spacing between point on the ESA. If the signals are 1 MHz apart then the ESA will not be able to resolve them. In this final case, the RBW remains 100 kHz; therefore, the DSA frequency spacing is still 38 kHz, so the DSA is able to resolve both signals.

In each of these cases, the DSA plots reveal a phenomenon that is occurring as a result of combining two signals. There are frequency components seen at the harmonics of the input signals which result from intermodulation distortion. Intermodulation distortion is a

Figure 4.12. Case 2 continued: Again, both the DSA and ESA resolve both signals, but the ESA reports the separation as an extra 10 MHz. The frequency axis is limited to display 300 MHz. The overall span is 6 GHz and the frequency separation is 70 MHz. (a) is the DSA FFT trace and (b) is the ESA trace. The data tips are included to show the discrepancy between the actual signal separation and the measured signal separation.
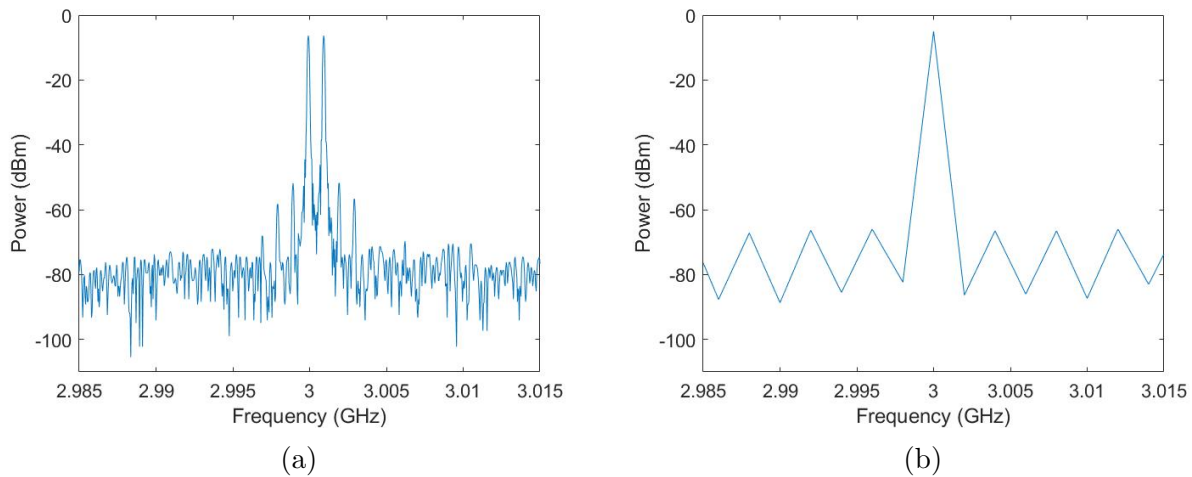

Figure 4.13. Case 3: Only the DSA can resolve both signals due to the 600 point limit of the ESA. (a) shows both of the frequencies resolved by the DSA. (b) shows only one signal resolved by the ESA.

non-linear process where the input frequency components are converted to harmonic powers. The result is intermodulation distortion that can be represented by: [25]

$$m\omega_1 + n\omega_2 \tag{4.19}$$

69

Based on the integer values of the harmonics, the frequency components are a result of second harmonic generation, sum frequency generation, or difference frequency generation[25]. For intermodulation distortion, the dominate harmonics are found at $2\omega_1 - \omega_2$ and $2\omega_2 - \omega_1$. Similarly, if the distortion is scaled by 3 dB when the input is changed by 1 dB then the distortion is caused by the measurement tool itself. The synthesizer's data sheet does illustrate this phenomenon when an RF combiner is utilized; however, the traces taken using the ESA do not exhibit the same distortion as seen in the DSA traces. Furthermore, the distortion on the DSA does not scale consistently as the input is increased; however, the increase in distortion is greater than 1, and depending on the input, can be 3 dB. The harmonics shown in the DSA plot are found at $2\omega_1 - \omega_2$, $2\omega_2 - \omega_1$, $3\omega_1 - 2\omega_2$, and $3\omega_2 - 2\omega_1$. As a result, the distortion can likely be attributed to intermodulation distortion in the DSA itself.

This experiment using preset frequency offsets shows that there are cases, when sweeping across a large span, that the DSA's increased memory depth and smaller frequency bin size can resolve signals that the ESA cannot. The DSA's frequency bin resolution is based on the sampling rate divided by the number of samples taken across the entire bandwidth. These two values can be adjusted manually to make the frequency bins smaller. The ESA's frequency bin resolution is determined by the total measurement span divided by 600 points, which limits the size of the frequency bins. This advantage will be further explored in the next section with a real APHI signal.

4.5.2 APHI Comb Experiments using the DSA and ESA

As described in Chapter 3, an octave spanning frequency comb is required in order to meet the requirements of the optical atomic clock. As a result, the repetition rate is in the THz range, which is too fast to be read by microwave electronics. For this reason, the repetition rate of the comb needs to be divided down further. In order to achieve this, two optical frequency combs are beat together, and the corresponding beat notes are mixed using an unbalanced RF mixer. The result of the mixing is three signals: the carrier frequency,

an upper sideband and a lower sideband (the sidebands are generated according to equation 4.11). One of the sidebands will contain the sum of frequency components, whereas the other will contain the difference of frequency components. Since there is noise present in each frequency measurement, the sideband with the sum of the frequency components will be more noisy (as the noise components add) whereas the sideband with the difference in frequency components will be less noisy as some frequency terms will cancel. The divided repetition rate is the difference term. A measurement using an RF instrument is required to determine which of the sidebands is the divided repetition rate. Figure 4.14 shows the repetition rate measurement taken by both the DSA and the ESA. Figure 4.14(a) displays a carrier frequency which has two sidebands. The carrier frequency (under the current comb configuration) is the optical atomic clock output. Figure 4.14 (b) and 4. 14(c) are the left and right sidebands respectively. These sideband figures are composed of the same data shown in the middle plot; however, the frequency axis limits were altered in order to emphasize the areas of interest and highlight the differences in the signals–but the data was not changed.

The figure shows that there are two sidebands. One of the sidebands (which is less noisy) is difference term, and the the divided repetition rate, whereas the other sideband is the noiser sum of the two signals frequency components. At this frequency scale, there are 333 kHz between each sample on the ESA trace, compared to 1.19 kHz between samples on the DSA. For this reason, the left and right sidebands of the ESA trace look nearly identical compared to the noise variations displayed by the DSA trace. Despite setting the RBW of the ESA to 3 kHz, the frequency point spacing negated the fine resolution bandwidth because the frequency bin spacing dominates the resolution capabilities. Any frequency discrepancies between the two sidebands can likely be attributed to two separate things: first, there was a time lapse between taking the ESA and DSA traces in which the comb system could have changed; and second, the finer resolution of the DSA placed the actual value of the signals in between the frequency samples of the ESA.

In addition, to the increased frequency resolution, the DSA also reduced the amount of time to take this measurement. Using these comparable resolution bandwidths, the ESA

took approximately a minute to sweep across the span (characterized by equation 4.12) and transfer the data to MATLAB compared to around 20 seconds, for the DSA to perform the same measurement using the FFT. This is important because the DSA reduced the amount of time that the operator needed to wait for this measurement to be completed. Furthermore, in order for the ESA to detect the noise difference between the two signals, two separate measurements (of each sideband) with a much reduced span would be required to identify which sideband is the repetition rate. The DSA is able to complete this measurement in a single trace which further reduces data collection time.

4.6   RF Instrumentation Conclusions

As shown by the noise floor experiments and the frequency resolution experiments, the DSA can be leveraged as a valuable tool for optical frequency comb and optical atomic clock experiments. The lower overall instrument noise floor and instrument noise figure of the DSA is an improvement of $\sim$10 dB over the ESA. In addition, the extensive memory depth of the DSA allows for better resolution which can serve as a valuable asset for large span measurements. If the separation between desired signals is large compared to the total measurement span divided by 600 points, than either the ESA or the DSA can be used for a measurement as both will resolve the signals. When the measurement separation is close to the 600 point limit of the span, then the operator will need to determine how much error they are willing to tolerate in their measurement when determining whether or not the DSA or ESA should be used. In general, the DSA possesses less discrepancy due to its smaller frequency resolution. Finally, if the measurement occurs within the frequency bin limitation of the ESA, then the DSA should be employed.
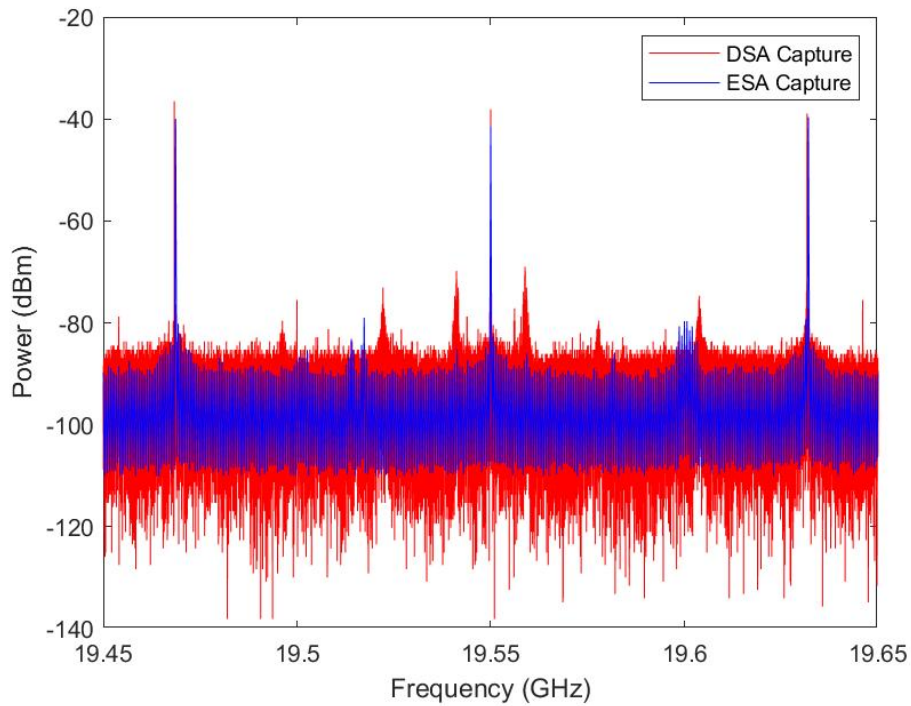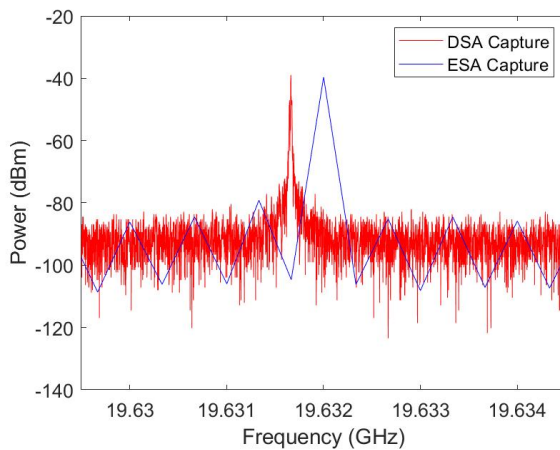
(a)
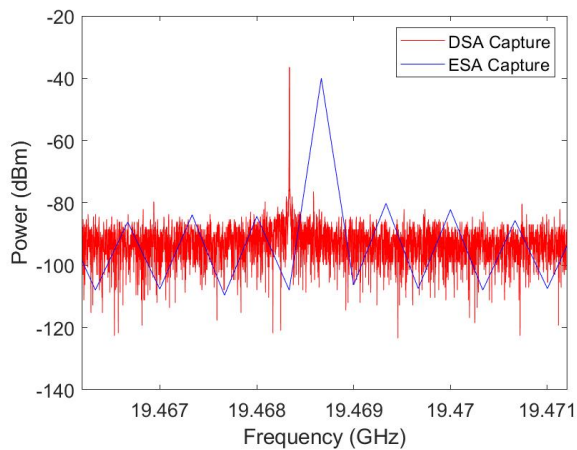
(b)

(c)

Figure 4.14. APHI divided repetition rate captured by both the DSA and ESA. (a) highlights the carrier and the sidebands that result from modulation. (b) zooms in on the lower sideband. (c) zooms in on the upper sideband. The DSA RBW was 2 kHz, the ESA RBW was 3 kHz.

5. CONCLUSION AND FUTURE WORK

This thesis focused on optical atomic clocks and the experiments being performed to implement this technology for defense applications. It highlighted how a complex defense capability, such as timing, can be broken down into an individual system (the optical atomic clock) which further breaks down to individual components (such as the optical frequency comb), and finally to the experiments described here.

Chapter 2 described the construction and testing of a 2 μm fiber laser that was used to test second harmonic devices. The laser possessed a limited tuning range of 54 nm from 1938 nm to 1992 nm. It also possessed a wavelength dependent output power between approximately 0 dBm and 8 dBm. The output power of the laser fluctuated over time due to polarization changes within the laser. Despite its limited tunable range and its power fluctuations, the laser was able to provide initial performance parameters of some of the second harmonic devices.

Chapter 3 described the testing and performance of the PPLN devices used for second harmonic generation and f-2f self-referencing. The goal of the experiment was to determine the center frequencies of many of the devices and evaluate the devices' second harmonic generation capabilities. Since the devices possess output frequencies near 1 μm, three different sources with light near 2 μm were utilized as inputs. These inputs included the fiber laser described in chapter 2, the amplified spontaneous emission profile of a thulium doped fiber amplifier, and a commercial 2 μm laser. Device C6D13 was chosen for use in the APHI comb system due to its center wavelength near 978 nm, its output power near -30 dBm, and its efficiency of $\sim$5%/W.

Chapter 4 described the interface and operation of RF measurement instruments. The chapter highlights the noise floors and noise figures of the Keysight DSA 93004L and the Aglient 8565EC ESA. The noise performance of the DSA is $\sim$10 dB better than the noise performance of the ESA. This chapter also characterizes the frequency bin resolution of the

two devices. The DSA's large memory depth reduces the size of its frequency bins, increasing its resolution. This is compared to the ESA's fixed number of points which makes the instrument's resolution dependent on the size of the measurement span. This chapter shows that the DSA can be a valuable asset for APHI program due to its improved noise floor compared to the ESA and its ability to resolve closely spaced signals across a large span as a result of its high sampling rate and large memory depth.

Some future work includes testing even more of the PPLN devices with center wavelengths outside of the built 2μm laser using the commercial Sacher laser. In addition, the capabilities of the DSA can be leveraged for even more APHI frequency comb measurements beyond the divided repetition rate measurement.

REFERENCES

[1] A. Bauch, "Caesium atomic clocks: Function, performance, and applications," *Measurement Science and Technology*, vol. 14, pp. 1159–1173, 2003. [Online]. Available: stacks.iop.org/MST/14/1159.

[2] S. Diddams, T. Udem, J. Bergquist, and et al, "An optical clock based on a single trapped ^{199}**hg**$^+$," *Science*, vol. 293, pp. 825–828, 2001. [Online]. Available: https://www.science.org/doi/10.1126/science.1061171.

[3] T. Schuldt, M. Gohlke, M. Oswald, and et al, "Optical clock technologies for global navigation satellite systems," *GPS Solutions*, vol. 25, no. 83, 2021. [Online]. Available: https://doi.org/10.1007/s10291-021-01113-2.

[4] P. Gill, H. Margolis, A. Curtis, and et al, "Optical atomic clocks for space," Hampton Road, Teddington, Middlesex, United Kingdom, Tech. Rep., version 1.7, 2008. [Online]. Available: https://www.researchgate.net/profile/Stephen-Lea-3/publication/241531359_Optical_Atomic_Clocks_for_Space/links/00b49534f8c78e4ec9000000/Optical-Atomic-Clocks-for-Space.pdf.

[5] Z. Newman, V. Maurice, T. Drake, and et al, "Architecture for the photonic integration of and optical atomic clock," *Optica*, vol. 6, no. 5, 2019. [Online]. Available: https://doi.org/10.1364/OPTICA.6.000680.

[6] A. Ludlow, M. Boyd, J. Ye, and et al, "Optical atomic clocks," *Reviews of Modern Physics*, vol. 87, 2015. DOI: 10.1103/RevModPhys.87.637.

[7] *Atomic-photonic integration (a-phi) broad agency announcement*, Defense Advanced Research Projects Agency, Jul. 25, 2018.

[8] E. Burt, J. Prestage, R. Tjoelker, and et al, "Demonstration of a trapped-ion atomic clock in space," *Nature*, vol. 595, 2021. [Online]. Available: https://doi.org/10.1038/s41586-021-03571-7.

[9] C. D. Matthias Lezius Tobias Wilken and et al., "Space-borne frequency comb metrology," *optica*, vol. 3, no. 12, 2016. [Online]. Available: https://opg.optica.org/optica/fulltext.cfm?uri=optica-3-12-1381&id=354726.

[10] T. Fortier and E. Baumann, "20 years of developments in optical frequency comb technologies and applications," *Communications Physics*, vol. 2, no. 153, 2019. [Online]. Available: https://doi.org/10.1038/s42005-019-0249-y.

[11] A. M. Weiner, *Ultrafast Optics*. Hoboken, New Jersey, USA: John Wiley and Sons, Inc, 2009, ISBN: 978-0-471-41539-8.

[12] Q.-F. Chen, A. Nevsky, M. Cardace, and et al, "A compact, robust, and transportable ultra-stable laser with a fractional frequency instability of 1×1015," *Review of Scientific Instruments*, vol. 85, no. 113107, 2014. [Online]. Available: https://doi.org/10.1063/1.4898334.

[13] T. Fortier, M. Kirchner, F. Quinlan, and et al, "Generation of ultrastable microwaves via optical frequency division," vol. 5, pp. 425–429, 2011. DOI: 10.1038/NPHOTON.2011.121.

[14] J. T. Verdeyen, *Laser Electronics*, 3rd. Englewood Cliffs, New Jersey, USA: Prentice Hall, 1995, ISBN: 0-13-706666-X.

[15] M. Gong, Y. Yuan, C. Li, and et al., "Numerical modeling of transverse mode competition in strongly pumped multimode fiber lasers and amplifiers," *Optics Express*, vol. 15, no. 6, 2007. [Online]. Available: https://doi.org/10.1364/OE.15.003236.

[16] J. Geng, Q. Wang, J. Wang, S. Jiang, and K. Hsu, "All-fiber wavelength-swept laser near 2μm," *Optics Letters*, vol. 36, no. 19, pp. 3771–3773, 2011.

[17] Z. Li, J. Daniel, A. Heidt, Y. Yung, S. Alam, and D. Richardson, "Thulium-doped fiber amplifier for optical communications at 2 μm," *Optics Express*, vol. 21, no. 8, 2013.

[18] J. Ding, B. Sampson, A. Carter, and et al, "A monolithic thulium doped single mode fiber laser with 1.5 ns pulsewidth and 8kw peak power," *Fiber Lasers VIII: Technology, Systems, and Applications*, vol. Proc. of SPIE Vol. 7914, 2011. DOI: 10.1117/12.876867.

[19] D. Jones, S. Diddams, J. Ranka, and et al, "Carrier-envelope phase control of femtosecond mode-locked lasers and direct optical frequency synthesis," *Science*, vol. 288, 2000. DOI: 10.1126/science.288.5466.635.

[20] Y. Jiang, Z. Bi, L. Robertsson, and L.-S. Ma, "A collinear self-referencing setup for control of the carrier-envelope offset frequency on ti:sapphire femtosecond laser frequency combs," *Metrologia*, vol. 42, pp. 304–307, 2005. DOI: 10.1088/0026-1394/42/4/016.

[21] R. Boyd, *Nonlinear Optics*. San Diego, CA, USA: Academic Press, Inc., 1992, ISBN: 0-12-121680-2.

[22] J. Wang, Y. Yu, Y.-M. Wei, and et al, "High-efficiency broadband second harmonic generation in single hexagonal gaas nanowire," *Scientific Reports*, vol. 7, no. 2166, 2017. DOI: 10.1038/s41598-017-02199-w.

[23] S. Zhang, W. Liu, Y. Jianghong, and et al, "Second harmonic generation in periodically poled lithium niobate waveguide using femtosecond laser pulses," *Proceedings of SPIE*, vol. 7135, 2008. DOI: 10.1117/12.803047.

[24] V. J. Urick, J. D. McKinney, and K. J. Williams, *Fundamentals of Microwave Photonics.* Hoboken, New Jersey, USA: John Wiley and Sons, Inc., 2015, ISBN: 978-1-118-29320-1.

[25] D. Pozar, *Microwave Electronics*, 3rd. Hoboken, New Jersey, USA: John Wiley and Sons, Inc., 2005, ISBN: 978-0-471-44878-5.

[26] *Application note 150: Spectrum analysis basics*, 2010. [Online]. Available: https://www.keysight.com/us/en/assets/7018-06714/application-notes/5952-0292.pdf.

[27] A. Oppenheim and A. Willsky, *Signals and Systems*, 2nd. Upper Saddle River, New Jersey, USA: Prentice-Hall, Inc., 1997, ISBN: 0-13-814757-4.

[28] R. Ziemer and W. Tranter, *Principles of Communications: Systems, Modulation, and Noise*, 7th. Hoboken, New Jersey, USA: John Wiley and Sons, Inc, 2015, ISBN: [978-1-118-07891-4.

[29] E. Ifeachor and B. Jervis, *Digital Signal Processing: A Practical Approach*, 2nd. Edinburgh Gate, England: Pearson Education Unlimited, 2002, ISBN: 0-201-59619-9.

[30] C. Holdenried, J. Haslett, J. McRory, and et al., "A dc-4 ghz true logarithmic amplifier: Theory and implementation," *IEEE Journal of Solid-State Circuits*, vol. 37, no. 10, pp. 1290–1299, 2002. DOI: 10.1109/JSSC.2002.803059.